

# Multicomponent bulk metal nitride ( $\text{Nb}_{1/3}\text{Ta}_{1/3}\text{Ti}_{1/3}\text{N}_{1-\delta}$ ) synthesis via reaction flash sintering and characterizations

Santanu Mondal<sup>1,2</sup>  | Andriy Durygin<sup>2</sup> | Vadym Drozd<sup>2</sup> | Jose Belisario<sup>1,2</sup> | Zhe Cheng<sup>1,2</sup> 

<sup>1</sup>Department of Mechanical and Materials Engineering, Florida International University, Miami, FL, USA

<sup>2</sup>Center for Study of Matter at Extreme Conditions (CeSMEC), Florida International University, Miami, FL, USA

## Correspondence

Zhe Cheng, Department of Mechanical and Materials Engineering, Florida International University, Miami, FL 33174, USA  
Email: zhcheng@fiu.edu

## Abstract

In this research, near fully dense single phase bulk multicomponent transition metal nitride ( $\text{Nb}_{1/3}\text{Ta}_{1/3}\text{Ti}_{1/3}\text{N}_{1-\delta}$ ) has been successfully synthesized from mixed commercial powders of NbN, TaN and TiN via reaction flash sintering technique. This was performed with an applied pressure of ~ 35 MPa at 25°C under a constant DC electric field (~24–32 V/cm). The flash event, which is the abrupt increase in current (up to ~ 25.2 A/mm<sup>2</sup>) and temperature, occurred without preheating. The threshold power dissipation on the sample right before the flash is ~ 0.7 W/mm<sup>3</sup>. The formation of single phase ( $\text{Nb}_{1/3}\text{Ta}_{1/3}\text{Ti}_{1/3}\text{N}_{1-\delta}$ ) random solid solution and its compositional uniformity were confirmed by XRD and EDS, respectively. The effects of ball milling duration and limiting current density on phase formation were studied. Simulation based on Joule heating provides an estimate of the ultimate sample temperature of ~ 1850°C. Vickers hardness of the obtained ( $\text{Nb}_{1/3}\text{Ta}_{1/3}\text{Ti}_{1/3}\text{N}_{1-\delta}$ ) is  $17.6 \pm 0.6$  GPa, which is comparable to similarly flash sintered ingredient binary nitrides of TaN and NbN. TGA in air shows that the oxidation resistance of ( $\text{Nb}_{1/3}\text{Ta}_{1/3}\text{Ti}_{1/3}\text{N}_{1-\delta}$ ) is better than that of TaN and NbN but inferior to TiN. The study demonstrates that reaction flash sintering can be a highly efficient technique for synthesizing bulk multicomponent ceramics for both material fundamental investigations and application development.

## KEY WORDS

density functional theory, flash sintering, hardness, nitride, oxidation resistance, phase transformations

## 1 | INTRODUCTION

Metal nitrides (such as TiN, TaN, and AlN) are excellent candidates for abrasion and corrosion resistant coatings,<sup>1–3</sup> diffusion barrier coatings,<sup>4–8</sup> and high temperature structural applications.<sup>9</sup> Recently multi-principle component nitrides, especially those based on transition metals (TM), have attracted significant research interest due to their excellent hardness,<sup>1,2,5,10</sup> superior chemical inertness,<sup>10</sup> decent electrical conductivity,<sup>11</sup> and robust thermal stability.<sup>12–16</sup>

So far, research on synthesizing multicomponent TM nitride has mainly been focused on thin film coatings, porous

structure, and fine powders.<sup>15–22</sup> To the best of the authors' knowledge, no research has been reported on the synthesis of dense bulk single phase multicomponent TM nitrides. In this work, a new bulk single phase multicomponent TM nitride, ( $\text{Nb}_{1/3}\text{Ta}_{1/3}\text{Ti}_{1/3}\text{N}_{1-\delta}$ ), is synthesized by a reaction flash sintering technique from three binary TM nitrides (ie, NbN, TaN and TiN). Flash sintering, first reported by Cologna et al,<sup>23</sup> is a sintering technique in which a green ceramic is densified quickly under the application of an electrical field (eg, ~7.5–1000 V/cm) at a lower surrounding temperature than other sintering techniques.<sup>24</sup> Various ceramic materials have been flash sintered, including YSZ,<sup>23,25</sup> ZnO,<sup>26–28</sup> CaCu<sub>3</sub>Ti<sub>4</sub>O<sub>12</sub>,<sup>29</sup>

$\text{MnCo}_2\text{O}_4$ ,<sup>30,31</sup>  $\text{La}_{0.6}\text{Sr}_{0.4}\text{Co}_{0.2}\text{Fe}_{0.8}\text{O}_3$ ,<sup>32</sup> and other oxide-containing ceramic composite materials.<sup>33–36</sup> Flash sintering has features such as very rapid increase in sample temperature ( $\sim 1000^\circ\text{C}/\text{min}$  or higher), very short sintering time (minutes down to even seconds), and high energy efficiency. In addition, in flash sintering, the electrical current only passes through the sample, and sample resistance drops dramatically with increasing temperature, possibly due to the formation of significantly higher concentration of defects.<sup>23,24,37</sup> Chemical reaction has also been incorporated into flash sintering to synthesize and densify multicomponent materials in one step.<sup>38,39</sup>

Despite the attractiveness of flash sintering, to the authors' best knowledge, flash sintering of TM nitride has not been reported yet, not to mention multicomponent TM nitrides. Therefore, in this research, reaction flash sintering technique is utilized to synthesize and also densify single phase  $(\text{Nb}_{1/3}\text{Ta}_{1/3}\text{Ti}_{1/3})\text{N}_{1-\delta}$  solid solution from three binary TM nitrides in one step. Phase analysis of the obtained material is carried out using XRD and Rietveld analysis. Sample microstructure and composition uniformity are characterized by SEM and EDS. Properties such as hardness and oxidation resistance of flash sintered  $(\text{Nb}_{1/3}\text{Ta}_{1/3}\text{Ti}_{1/3})\text{N}_{1-\delta}$  are also investigated. The results are compared with similarly flash sintered individual binary TM nitrides of NbN, TaN, and TiN as well as predictions from first principle calculations. This study is expected to help research in the efficient and low-cost processing of other bulk phase multicomponent (including high entropy) ceramics such as metal carbides and borides.

## 2 | EXPERIMENTAL PROCEDURE

### 2.1 | Raw materials and processing

For this research, commercial powders of niobium nitride (NbN, 99.5%, –325mesh, Alfa Aesar 12146), tantalum nitride (TaN, 99.5%, –325mesh, Alfa Aesar 13093), and titanium nitride (TiN, 99.5%, –10  $\mu\text{m}$ , Alfa Aesar 41556) were utilized as the starting materials to synthesize bulk single phase  $(\text{Nb}_{1/3}\text{Ta}_{1/3}\text{Ti}_{1/3})\text{N}_{1-\delta}$ . The three nitride powders were weighed to an equimolar proportion and mixed in a planetary ball mill (Retsch PM100, Retsch GmbH) using tungsten carbide lined aluminum jar and tungsten carbide milling media of 10 mm diameter for different durations (eg, 10 minutes, 1 hour, 2 hours, 5 hours, and 24 hours) under dry condition in air. The milling machine was programmed to have an intermittent schedule of 10 minutes of ball milling with 1 minute cooling for all the batches to minimize overheating and formation of oxides.

The ball milled mixtures (typically  $\sim 120$  mg) were uniaxially pressed at  $\sim 44$  MPa in a double inserted steel die into cylindrical pellets with diameter of 3.1 mm and thickness of  $\sim 2.5$  mm. The powder compaction helps improve particle

contacts and reduce electrical resistance; it also enhances diffusion and reactions to promote solid solution formation. The average bulk density after dry pressing was  $\sim 6.0$  g/cm<sup>3</sup> (estimated from sample weight and measured dimension) and relative density was  $\sim 62\%$ . (The theoretical density of the uniaxially pressed pallet is  $\sim 9.65$  g/cm<sup>3</sup>, as estimated from the consideration that it is an equimolar mixture of NbN, TaN, and TiN). The powder compaction was conducted without any organic binder to avoid the burnout stage before (reaction) flash sintering.

### 2.2 | Flash sintering setup and parameters

All flash sintering experiments were carried out in a home-made setup in air without any protective atmosphere. Figure 1A,B show the schematic and engineering drawing of the sample assembly for flash sintering. The prepressed powder compact (eg, NbN–TaN–TiN powder mixture) was placed in a hexagonal boron nitride (hBN) tube with an inner diameter (ID) of 3.1 mm, outer diameter (OD) of 6.0 mm, and length of 15 mm (labeled as hBN inner tube; it is machined out of 6.0 mm OD solid hBN rod). Two graphite rods with an OD of 3.1 mm and length of 7.5 mm were inserted into the hBN inner tube as the two electrodes contacting the nitride sample, and they are labeled as Graphite Inner Electrode. The hBN inner tube containing the powder compact and the two 3.1-mm OD graphite inner electrodes were together inserted into another hBN tube with an ID of 6.0 mm and OD of 12.1 mm and length of 50 mm (labeled as hBN outer tube in the schematic). Then, two graphite outer electrodes with 6.0 mm diameter on one side and 25.4 mm diameter on the other side were inserted into the hBN outer tube (with 6.0 mm ID) to provide current pathway. Finally, in order to minimize heat loss during flash sintering and also provide compressive constraint to the hBN outer tube (to prevent it from cracking), all of the above (ie, sample, hBN inner tube, hBN outer tube, together with the 3 mm diameter graphite inner electrodes, and the 6.0 mm/25.4 mm diameter graphite outer electrodes) were inserted into a graphite tube with an ID of 12.1 mm, OD of 25.4 mm, and length of 50 mm. Graphite is used for the outer tube because it is cheaper and easier to machine, and it handles thermal shock better than other materials such as aluminum oxide. Because the hBN tubes used are electrically insulating, during (reaction) flash sintering, all current only passes through the metal nitride(s) ceramic specimen and not the outer graphite tube. A pneumatic cylinder (as shown in Figure 1A) with input air pressure of 34 kPa and diameter of  $\sim 100$  mm was used to apply a constant compressive force upon the sample assembly, which results in an average pressure of  $\sim 35$  MPa upon the 3.1 mm diameter sample (assuming negligible friction). The applied pressure helps to maintain a stable electrical conduction path during the

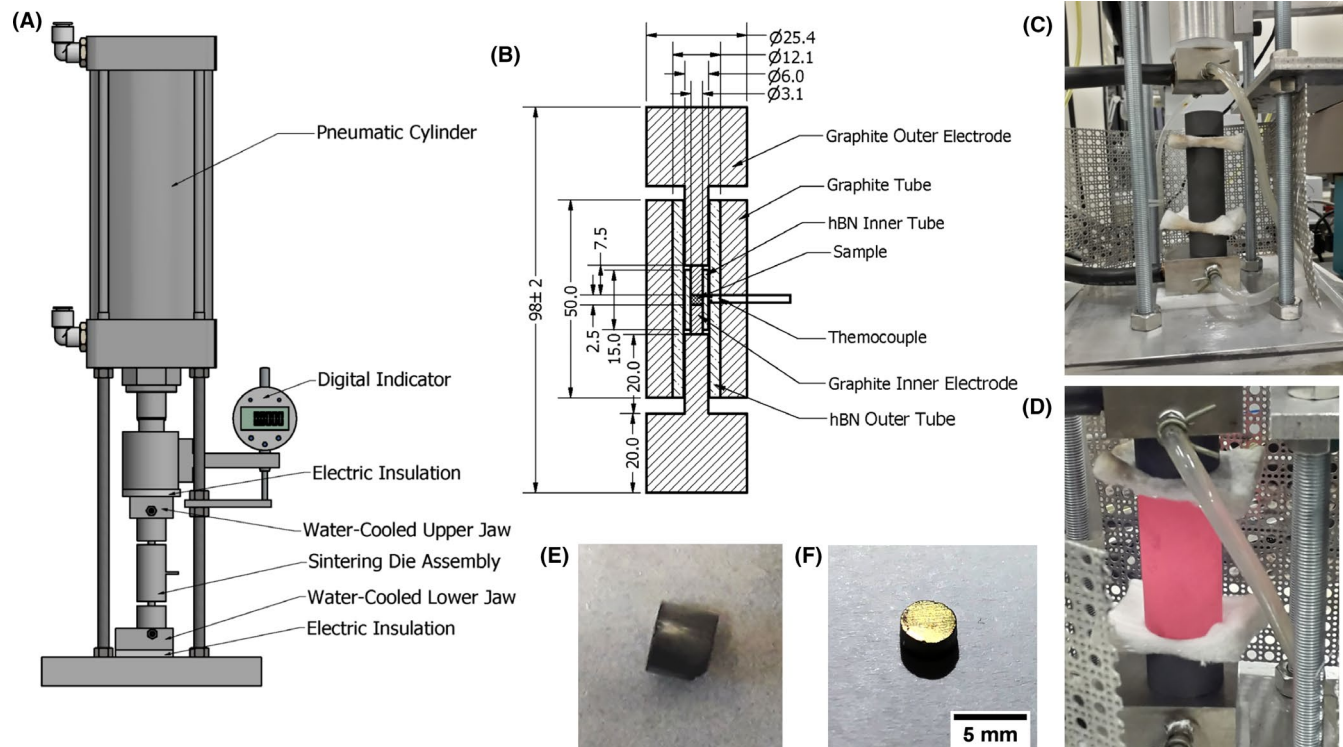


**FIGURE 1** A, Schematic diagram of the (reaction) flash sintering setup containing a pneumatic cylinder, a digital indicator, and the sample assembly. B, Engineering drawing of the (reaction) flash sintering sample assembly. C, Photo showing the setup before the flash sintering experiment. D, Photo showing the setup during a typical flash sintering experiment. (Note that although no current passes through the outer graphite tube, the intensive heating of the sample at the center of the assembly still caused the outer graphite tube to turn red hot (temperature  $\sim 1200^{\circ}\text{C}$ ). This needs to be managed in future through better thermal insulation and enclosure in an inert atmosphere chamber.) E, Photo of a green pellet of NbN-TaN-TiN powder mixture before reaction flash sintering. F, Photo of a reaction flash sintered ( $\text{Nb}_{1/3}\text{TaN}_{1/3}\text{Ti}_{1/3}\text{N}_{1-\delta}$ ) sample ground and polished slightly to show the golden metallic reflection [Color figure can be viewed at [wileyonlinelibrary.com](http://wileyonlinelibrary.com)]

flash sintering process. A digital indicator (Neoteck DTI digital dial indicator, resolution of 0.001 mm) with microcontroller-based computer interface is mounted on the piston side of pneumatic press to monitor displacement, which provides continuous reading about the change in sample dimension (in this case, thickness) during flash sintering.

All flash sintering experiments were carried out at ambient temperature (ie, without preheating of the sample) using a DC power supply (Hewlett Packard Model 6671A, 8 V, 220 A). With an applied pressure of 35 MPa, upon the application of constant DC voltage (typically 8 V or  $\sim 32 \text{ V/cm}$ ), the current increases rapidly, resulting in the flash event—the auto acceleration of current increase. As a result, the sample heats up quickly, which is accompanied by rapid shrinkage. Similar to a typical flash sintering experiment, when the current increases to a preset limit value  $I_{\text{lim}}$  (eg, 150, 170, and 190 A), the power source automatically switches from voltage control to constant current mode at  $I_{\text{lim}}$ . After running at  $I_{\text{lim}}$  for 120 seconds, the power supply switches off and the sample assembly cools down naturally.

It should be mentioned that in this study, although the flash sintering setup was in *open air*, the cylindrical nitride sample was enclosed inside the hBN tubes (inner and outer) and

sandwiched between the top and the bottom graphite electrodes, all of which were then contained by the outer graphite tube. As a result of such a multilayered assembly, the sample was protected from air oxidation during the (reaction) flash sintering despite the high sample temperature, as confirmed by XRD (see discussion later). We also want to mention that during the (reaction) flash sintering experiments, the outer graphite tube did become *red hot* (as will be discussed later in Section 3.2.3, the temperature for the *outer* surface of the graphite tube was estimated to be  $\sim 1200^{\circ}\text{C}$ , based on preliminary simulation work, see Figure 1D), which is a limitation with the present set up. We will try to address it in the future by providing inert atmosphere protection through containing the hot section of the assembly.

In order to estimate the ultimate sample temperature during flash sintering, simulation was carried out using COMSOL Multiphysics package (version-4.3). Due to the lack of literature data on physical properties (eg, electrical resistivity and thermal conductivity) for the starting mixture and the final product, as a first approximation, the simulation was performed by assuming the values for the three-metal nitride solid solution are the same as graphite. Other parameters used for the simulation are presented in Table S3 in the supporting document.

## 2.3 | Material characterization

The flash sintered samples (ie,  $(Nb_{1/3}Ta_{1/3}Ti_{1/3})N_{1-\delta}$  as well as individual binary nitrides) were ground to remove graphite from the contacting graphite electrodes using 60 grit SiC abrasive paper and then polished. The bulk density of the sintered samples was calculated from sample weight and measured dimension. A Siemens D-5000 X-ray diffractometer with  $CuK\alpha$  radiation source ( $\lambda = 1.54178 \text{ \AA}$ ) was employed for phase analysis. XRD pattern for Rietveld refinement was collected on a different Bruker D8 QUEST system equipped with a TRIUMPH curved-crystal monochromator and a  $Mo-K\alpha$  fine-focus X-ray radiation ( $\lambda = 0.71073 \text{ \AA}$ ). Collected 2D diffraction image was integrated using FIT2D software (version-12.012). Rietveld refinement of XRD pattern was performed using GSAS-1 software.

Scanning electron microscopy (SEM) was conducted on a JEOL 6330F FE-SEM (JEOL Ltd.) to examine the morphology of initial powders and also microstructure of the sintered pellets. Energy disperse X-Ray spectroscopy (EDS) analysis was carried out using an UltraDry EDS Detector (Thermo Fisher) to examine sample compositional uniformity after reaction flash sintering.

Vickers hardness was measured using a LECO LM810AT (LECO Corporation) with a Vickers diamond indenter at 2000 gf load and a hold time of 10 seconds. The hardness measurements were conducted according to the ASTM C1327 standard. To minimize experimental error, multiple measurements were taken at different locations for each specimen. Thermal gravimetric analysis (TGA) was carried out for fractured (reaction) flash sintered sample pieces using a simultaneous thermal analyzer (SDT Q600, TA instrument) in dry air from room temperature to  $1300^\circ\text{C}$ . The air flow rate was  $100 \text{ cm}^3/\text{min}$  and the heating rate was  $10^\circ\text{C}/\text{min}$ .

## 2.4 | First principle calculations

To provide some theoretical guidance about the target random solid solution of  $(Nb_{1/3}Ta_{1/3}Ti_{1/3})N_{1-\delta}$ , first principle calculation was also carried out using the supercell approach. The Special Quasi-Random Structure (SQS) method<sup>40</sup> is commonly used to model the disordered structure of metal alloys. In this study, SQS supercell of  $(Nb_{1/3}Ta_{1/3}Ti_{1/3})N_{1-\delta}$  random multicomponent nitride containing 36 atoms (18 nitrogen and 18 total metal atoms) was generated by using Alloy-Theoretic Automated Toolkit (ATAT).<sup>41</sup> Relaxed supercell of  $(Nb_{1/3}Ta_{1/3}Ti_{1/3})N_{1-\delta}$  is shown in Figure S3. Density functional theory (DFT) calculations were performed using Vienna ab initio simulation package (VASP).<sup>42,43</sup> The generalized gradient approximation (GGA)<sup>44</sup> with the Perdew-Burke-Ernzerhof (PBE) exchange-correlation functional<sup>45</sup> was used to describe exchange and correlation effects.

Electron wave functions were expanded by plane wave with a high enough cutoff energy of 520 eV. To obtain the total energy, Monkhorst-Pack<sup>46</sup>  $k$ -point meshes with density not less than 1000 pra (per-reciprocal-atom) were used to sample the Brillouin zones. Both cutoff energy and  $k$ -point mesh were tested to sufficiently achieve a high accuracy atomic relaxation until the change in total energy was less than 0.01 meV, and all the forces on each atom were smaller than 0.01 eV/ $\text{\AA}$ . Generated SQS unit cell were relaxed in three steps: (a) only the cell volume was relaxed; (b) both cell shape and volume were relaxed; (c) atomic positions, cell shape and volumes were allowed to relax. Final total energy was obtained from a static calculation, shown in Table S2.

Elastic constants (ie, Young's modulus  $E$ , shear modulus  $G$ , and bulk modulus  $B$ ) of the nitride ceramics were calculated by determining the Hessian matrix (matrix of the second derivatives of the energy with respect to the atomic positions) as it is implemented in VASP starting from version 5.1. Six finite distortions of the lattice are performed and the elastic constants are derived from the strain-stress relationship from elastic tensor using script ELATE.<sup>47</sup> Values calculated using Hill method, which is considered as average of upper (Voight) and lower (Reuss) bounds, are reported. Because elastic constant calculation needs accurate structural relaxation to a state of approximately zero stress, more precise DFT parameters compared to a total energy-calculation were employed.<sup>48</sup> Specifically, for elastic properties calculations, cutoff energy and density of  $k$ -points mesh were increased to 700 eV and 7000 pra, respectively.

## 3 | RESULTS AND DISCUSSION

### 3.1 | Characterization of binary nitrides and their powder mixture prior to (reaction) flash sintering

XRD analysis (see Figure 2) shows that the as-received NbN powder is mostly cubic phase (ICCD-PDF-4 card number 04-004-2895) with a very little amount of hexagonal phase (ICCD-PDF-4 card number 01-089-2908); TaN contains a mixture of at least two phases: the majority is hexagonal TaN (ICCD-PDF-4 card number 00-039-1485) and the minor phase matches best with  $Ta_5N_6$  (ICCD-PDF-4 card number 04-012-7243); TiN is cubic phase (ICCD-PDF-4 card number 04-002-1925). SEM (see Figure S1) shows that the particle size is large and the size distribution is broad for all three commercial powders:  $<\sim 30 \mu\text{m}$  for NbN,  $<\sim 45 \mu\text{m}$  for TaN, and  $<\sim 20 \mu\text{m}$  for TiN, respectively.

As mentioned, ball milling was used for mixing the three binary nitride powders and also reducing the particle size. Figure 2 also shows the XRD patterns for the equimolar mixture of NbN, TaN, and TiN powders after ball milling for

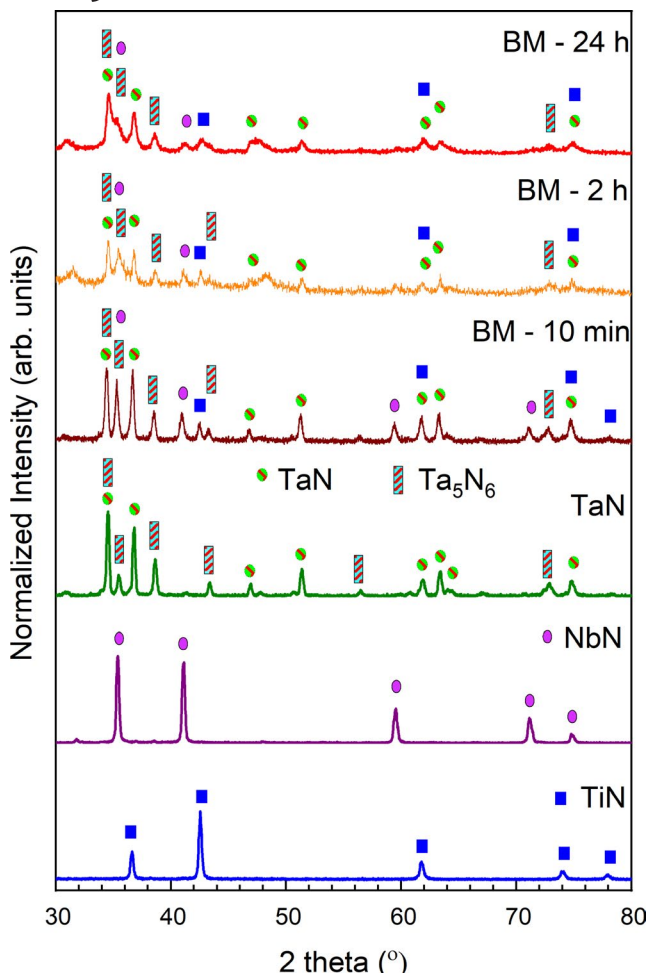


**FIGURE 2** XRD patterns of the as-received commercial TiN, NbN, TaN powder and the NbN-TaN-TiN powder mixtures after ball milling (BM) for 10 min, 2 h, and 24 h [Color figure can be viewed at wileyonlinelibrary.com]

10 minutes, 2 hours, and 24 hours. Longer ball milling time leads to broadening and partial merging of the XRD peaks. (See Table S1 for a summary of the measured full width at half maximum (FWHM) for selected peak of each individual ingredient nitride before and after 10 minutes, 2 hours and 24 hours ball milling for mixing.) Such observations indicate loss or crystallinity, which is attributed to the combined effects of reduction in particle size, incorporation of strain in the milled material, and, possibly, (partial) mechanochemical alloying.

### 3.2 | Reaction flash sintering and simulation for heat generation and distribution

#### 3.2.1 | A representative reaction flash sintering process

Figure 1C,D are photos of the homemade setup before and during the reaction flash sintering experiment. During the

flash sintering process, the sample assembly within the outer graphite tube got red hot. However, it should be emphasized again that all current only passed through the sample and not through the outer graphite tube because that graphite tube is electrically isolated from both the top and bottom graphite electrodes and the sample by the insulating hBN tubes (see schematic in Figure 1B). The graphite tube only became hot through heat radiation and conduction from the sample at the center of the assembly. As mentioned earlier that the outer graphite tube gets red hot during (reaction) flash sintering (and possibly experiences graphite oxidation) is a limitation for the current setup, and modification will be implemented in future to address this issue.

Figure 1E,F are representative pictures of the NbN-TaN-TiN powder mixture compact before and after reaction flash sintering. As shown in Figure 1F, the sample after reaction flash sintering was ground and polished slightly and it shows golden metallic reflection from the surface. As stated before, although the (reaciton) flash sintering experiments were carried out in air, the samples are protected from oxidation (also see later discussion on phase formation), presumably because they are enclosed within the multilayer assembly made of inert hBN tubes and graphite electrodes.

Figure 3 shows the typical reaction flash sintering process capturing the current passing through the sample, the displacement of the top electrode with respect to the bottom electrode was measured from the digital indicator, and the temperature measured from the inserted thermocouple touching the hBN inner tube (ie, ~1.5 mm from the sample surface), all as a function of time, for a Nb-Ta-Ti three-metal nitride sample. The limiting current  $I_{\text{lim}}$  in this case was 190 A and the applied pressure was ~35 MPa, as stated. The flash event occurred at ambient temperature (ie, 25°C) without any preheating as soon as the constant 8 V of DC voltage was applied. Specifically, even for the first data point collected at ~0.6 seconds, the measured current was already ~12 A (~1.6 A/mm<sup>2</sup>). The current then increased rapidly by more than ~15 times to ~190A (~25.2 A/mm<sup>2</sup>) in ~30 seconds. Consequently, the electrical power dissipation for the entire sample assembly increased from 96 W at ~0.6 seconds to 1520 W at ~30 seconds.

As a result of the high power dissipation, the sample heated up and the measured temperature increased rapidly (> ~500°C/min). Meanwhile, the sample experienced minor expansion initially (up to ~20 seconds with thermocouple reading of ~400°C) followed by rapid shrinkage, which was associated with densification caused by Joule heating as well as the applied external pressure (~35 MPa), as in sinter-forging.<sup>49</sup> When current increased to the preset limit  $I_{\text{lim}}$  of 190 A (~25.2 A/mm<sup>2</sup>), the power source switched to constant current mode and maintained at  $I_{\text{lim}}$  for 120 seconds. During this time (from ~80 to 200 seconds), the measured temperature continued to increase but at a slower rate, while the overall

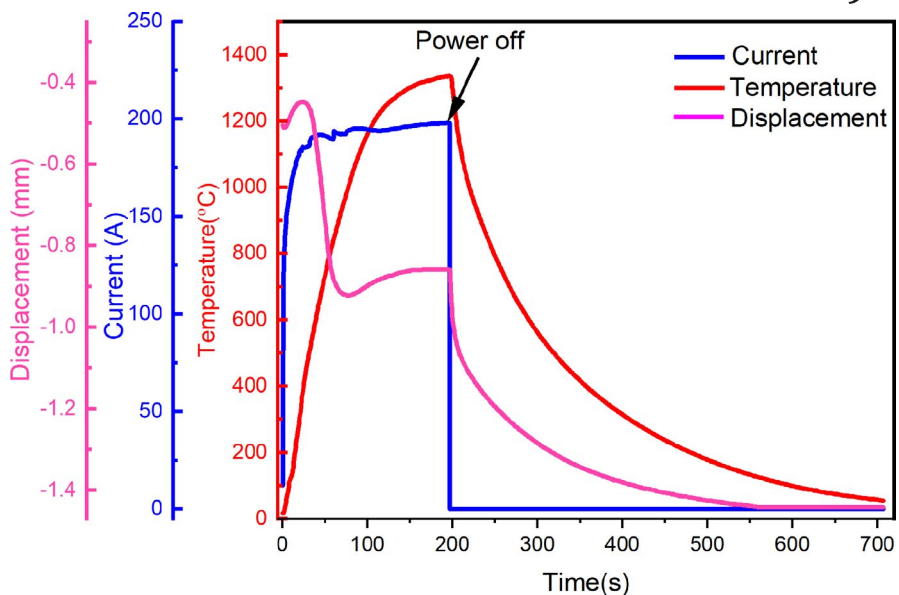


**FIGURE 3** Representative plots of current, displacement of the top electrode with respect to the bottom electrode, as well as measured temperature versus time for a typical reaction flash sintering of the NbN–TaN–TiN equimolar powder mixture after ball milling for 2 hours. The applied pressure was ~35 MPa, the initial DC voltage was 8 V (or ~32 V/cm), and there was no sample preheating. The system ran under constant voltage mode until current reached the preset limit  $I_{\text{lim}}$  of 190 A when the power supply switched to constant current mode and hold for 120 seconds. Note that because the thermocouple only touched the outside of the hBN inner tube, the measured temperature would be significantly lower than actual sample temperature [Color figure can be viewed at wileyonlinelibrary.com]

sample appeared to *expand* slowly. Such expansion (at ~80–150 seconds) does not necessarily mean the sample densification is completed right when the power supply switches to the constant current mode. It is possible that the shrinkage due to densification and thermal expansion work against each other, and the net effect during this period is slight expansion. Finally, after ~150 seconds, the sample dimension stabilized, meaning the sample reached full densification, while the system also approached maximum possible temperature as determined by thermal equilibrium. Table 1 provides a summary of major samples' (reaction) flash sintering limiting current, the measured relative density, and their Vickers hardness. The (reaction) flash sintered samples show high relative density and decent hardness, which will be discussed in detail later.

In terms of sample resistance during the reaction flash sintering process, when the applied voltage was 8 V, at the very beginning (~0.6 seconds), it was ~0.65 Ω (8 V/12 A minus 0.02 Ω for the two 7.5 mm long, 3.1 mm diameter graphite electrodes<sup>50</sup>). After flash, it decreased by 30 times to ~0.021 Ω under steady state (8 V/190 A minus ~0.02 Ω for the two graphite electrodes. Literature suggest that graphite resistivity shows very small change between room temperature and 2000°C<sup>50</sup>).

Consider that the sample has a diameter of 3.1 mm and initial thickness of ~2.5 mm, the power density (ie, power dissipation per unit volume) on the sample at the beginning was  $(12 \text{ A})^2 \times 0.65 \Omega / 18.8 \text{ mm}^3 \approx 5 \text{ W/mm}^3$ , and it increased to as high as ~50 W/mm<sup>3</sup> ( $(190 \text{ A})^2 \times 0.021 \Omega / 15.1 \text{ mm}^3$ , since sample thickness shrank to ~2.0 mm) after reaching

steady state. The power density is very high compared with other materials,<sup>51</sup> and more discussion on the change in sample resistance and powder density in the reaction flash sintering of nitride samples will be given in the following section.

It should be mentioned that the energy consumption appears high (eg,  $190 \text{ A} \times 8 \text{ V} \times 120 \text{ seconds} = 182\,400 \text{ J}$ ) compared to some other reported flash sintering results. The higher energy consumption reported here is attributed to the fact that in the present flash sintering experiment, there is *no*

**TABLE 1** Summary of limiting current  $I_{\text{lim}}$ , measured relative density, and Vickers hardness for selected (reaction) flash sintered samples in this study. All samples had a diameter of ~3.1 mm and were (reaction) flash sintered with initial DC voltage of 8 V before reaching  $I_{\text{lim}}$ . The relative density was calculated based on a theoretical density of 8.47 gm/cm<sup>3</sup> for NbN, 15.40 gm/cm<sup>3</sup> for TaN, and 5.40 gm/cm<sup>3</sup> for TiN. The theoretical density for the three-metal nitride is calculated to be 9.57 gm/cm<sup>3</sup> based on a lattice parameter of 4.3400(3) Å from Rietveld analysis

Sample	Limiting current $I_{\text{lim}}$ (A)	Relative density (%)	Vickers hardness (GPa)
	190	99	$17.7 \pm 0.6$
$(\text{Nb}_{1/3}\text{TaN}_{1/3}\text{Ti}_{1/3})\text{N}_{1-\delta}$	170	94	$14.6 \pm 0.4$
	150	83	$9.8 \pm 0.5$
NbN	190	96	$16.9 \pm 0.5$
TaN	190	95	$18.9 \pm 1.9$
TiN	190	88	$13.2 \pm 0.4$

*preheating*. As a result, a large portion (probably majority) of generated heat in the sample is dissipated to the surrounding parts (eg, hBN inner and outer tubes, graphite electrodes, and graphite tube) and the environment, which are initially all at room temperature. In comparison, in (some) other flash sintering experiments involving high temperature materials such as 3YSZ, the samples are kept at elevated temperature (eg, inside a furnace of  $\sim 850^{\circ}\text{C}$  or higher) before the flash event.<sup>23</sup> Therefore, there is naturally much more significant heat loss for the current setup comparing with other flash sintering. In the future research, we will modify the flash sintering setup to try to reduce the heat loss. We will also explore more about the effect of holding time and see if shorter hold time will lead to adequate densification. These might help to improve the energy efficiency for the reaction flash sintering process.

### 3.2.2 | Incubation stage before flash event with lower applied DC voltage

It is noted that for the reaction flash sintering experiment described above, the initial applied 8 V DC voltage, though efficient to trigger the flash event in a timely fashion, might be too high: This is because in Figure 3, there seemed to be *no incubation* stage, which is typically the 1st stage with low current and low power in flash sintering experiments *before* the 2nd stage of flash or the so-called transient stage.

To better characterize and understand the onset of flash or the transition from the 1st stage incubation to 2nd stage flash, additional experiments had been carried out. Specifically, in another experiment, all conditions (eg, sample type and geometry and also no preheating) were kept the same except that the initial DC voltage applied was 6 V instead of 8 V. The results are shown in Figure S4 of the supporting document. In this case, the initial current (at the first point taken at  $\sim 0.6$  seconds) recorded was only  $\sim 0.15$  A. As the voltage was ramped up at 5 mV/s, the current increased, first very slowly till  $\sim 2$  A at  $\sim 188$  seconds (under  $\sim 6.94$  V), then it increased almost exponentially within 4 seconds to  $\sim 80$  A at  $\sim 192$  seconds (under  $\sim 6.96$  V, see Figure S4A,B). After that, the current still increased with increasing voltage, but not as dramatically.

In terms of resistance, this second experiment shows the sample apparent resistance was  $\sim 40$   $\Omega$  (6 V/0.15 A, assuming negligible contact resistance between graphite electrodes and the sample) at the beginning (time of  $\sim 0.6$  seconds), and it decreased to 3.45  $\Omega$  ( $6.94$  V/2 A minus the graphite electrodes' total resistance of  $\sim 0.02$   $\Omega$ ) at 188 seconds. Then within just 4 seconds, the sample resistance decreased by another  $\sim 50$  times to 0.067  $\Omega$  ( $6.96$  V/80 A minus the graphite electrodes' total resistance of  $\sim 0.02$   $\Omega$ ) at 192 seconds. The total drop in resistance from the beginning was  $\sim 600$  times. Such a large drop in sample effective resistance is characteristic of "flash sintering" phenomena reported in the literature.<sup>52</sup>

In terms of power density, as discussed in earlier section, when the DC voltage applied was 8 V, the initial power density on the sample even for the first data point ( $\sim 0.6$  seconds) was 5 W/mm<sup>3</sup>, which seems too high as the threshold power to trigger the flash event.<sup>52</sup> For the second experiment as shown in Figure S4, at the beginning when 6 V was just applied ( $\sim 0.6$  seconds), the graphite electrode resistance (estimated to be  $\sim 0.02$   $\Omega$ ) is much lower than the sample. The power dissipation on the sample would be  $(0.15\text{ A})^2 \times 40\text{ } \Omega = 0.9\text{ W}$ . Therefore, the power density at the *very beginning* is  $0.9\text{ W}/18.8\text{ mm}^3 = \sim 0.05\text{ W/mm}^3$ . Right before the flash (approximately the point at 188 seconds with  $\sim 6.94$  V and  $\sim 2$  A), as stated, the sample resistance was 3.45  $\Omega$  (still neglecting the contact resistance). The total power dissipation on the sample would be  $(2\text{ A})^2 \times 3.45\text{ } \Omega = 13.8\text{ W}$ . Therefore, the *critical orthreshold power density right before flash* would be  $13.8\text{ W}/18.8\text{ mm}^3 = 0.7\text{ W/mm}^3$ .

The above threshold power density of 0.7 W/mm<sup>3</sup> still seems higher than the typical critical values for flash sintering of oxide ceramics ( $\sim 0.01\text{--}0.05\text{ W/mm}^3$ ).<sup>51</sup> This might be attributed to the lower resistivity for the nitride materials used. Specifically, the electrical resistivity of TiN, TaN and NbN (all reported for coatings) are summarized here: TiN varies from  $2.7 \times 10^{-5}$  to  $30 \times 10^{-5}$   $\Omega\cdot\text{cm}$ ,<sup>11,53,54</sup> TaN varies from  $0.1 \times 10^{-5}$  to  $1.4 \times 10^{-5}$   $\Omega\cdot\text{cm}$ ,<sup>55,56</sup> and NbN varies from  $0.5 \times 10^{-5}$  to  $60 \times 10^{-5}$   $\Omega\cdot\text{cm}$ <sup>11,57,58</sup> depending on preparation condition, grain size, and metal to N ratio in the specimen. Though the values vary, they all appear much lower than most oxides studied for flash sintering.

However, it should be mentioned that for the reaction flash sintering experiment with 6 V DC, the *effective resistivity* for the green sample compact initially (with 0.15 A initial current) is estimated to be  $\sim 11\text{ }\Omega\cdot\text{cm}$ , which is five to six orders of magnitude higher than the reported binary TM nitrides' intrinsic resistivity at room temperature. The origin for this large gap between the low intrinsic resistivity of nitrides and the high effective resistivity for the compacted, ball milled mixture from the three TM nitrides is not likely due to sample porosity ( $\sim 40\%$ ) alone before reaction flash sintering. It may be related to surface oxides covering the TM nitride powders or other effects, and further study is required to clarify on this important issue.

### 3.2.3 | Simulation for heat generation and distribution

Because of the difficulties in measuring the actual sample temperature during reaction flash sintering (the thermocouple only touches the hBN inner tube and the type R thermocouple available will melt upon reaching  $\sim 1750^{\circ}\text{C}$ ), heat generation and temperature distribution were simulated with COMSOL Multiphysics-4.3 package. As stated, due to the lack of literature data, the physical properties of the three-metal nitride

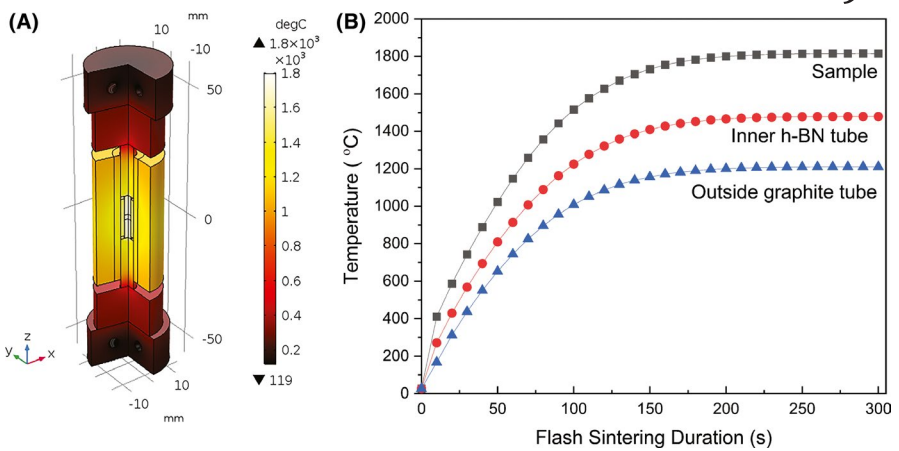


**FIGURE 4** A, A representative heat distribution profile for the sample assembly during the reaction flash sintering as obtained via COMSOL simulation. It represents the condition after running under a constant voltage of 8 V for 200 seconds. B, Plot of simulated temperature versus time for three different locations within the sample assembly during the reaction flash sintering process under 8 V constant applied DC voltage. The black square is for the sample center; the red circle represents the position of the thermocouple tip, which is touching the outer surface of the hBN inner tube ( $\sim 1.5$  mm from the sample surface); the blue triangle is for the outer surface of the graphite tube. The major parameters for the simulation are provided in Table S3 of the supporting document [Color figure can be viewed at wileyonlinelibrary.com]

were assumed to take the values of graphite. Figure 4A shows the simulated temperature profile after the 8 V DC voltage is applied for 200 seconds. The maximum temperature at the center is  $\sim 1850^\circ\text{C}$ , while the temperature measured from the thermocouple is only  $\sim 1340^\circ\text{C}$ . To help understand the difference, Figure 4B shows the change of temperature versus time at different locations within the sample assembly—at the sample center, on the surface of the hBN inner tube where the thermocouple tip is located, and at the outside surface of the graphite tube. It shows that the temperature at the inner hBN tube (red circle) is much lower than the sample center (black square) and matches with the measured value reasonably.

Also, we would like to mention that although the melting point for the three-metal nitride has not yet been determined, it is expected to be slightly lower than the lowest melting point, which is for NbN at  $2573^\circ\text{C}$  or 2846 K. As a first approximation, if taking 2846 K as the melting point for the three-metal nitride, then the modeled sample peak temperature of  $1850^\circ\text{C}$  (see Figure 4) would be at  $2123/2846 \approx 0.74$  of the melting temperature. This seems reasonable for flash sintering. In fact, such a ratio is consistent with the reported flash sintering for 3YSZ: Its melting point is  $\sim 3000$  K, while the modeled peak temperature during 3YSZ flash sintering is  $\sim 1900^\circ\text{C}$ , and the ratio to melting point would be  $2173/3000 \approx 0.72$ .<sup>52,59</sup>

### 3.3 | Formation of single phase $(\text{Nb}_{1/3}\text{Ta}_{1/3}\text{Ti}_{1/3})\text{N}_{1-\delta}$ random solid solution after reaction flash sintering

Figure 5A shows XRD of the NbN–TaN–TiN equimolar mixture sample after 2 hours of ball milling and then reaction

flash sintering ( $I_{\text{lim}} = 190$  A). For comparison, the XRD patterns for the three individual binary nitrides after going through similar flash sintering (same  $I_{\text{lim}}$  of 190 A) are also plotted. As mentioned, before flash sintering, the as-received TiN was pure cubic phase, NbN was cubic phase with a very little amount of hexagonal phase, but the as-received nominal “TaN” (from Alfa Aesar) was in fact a mixture of hexagonal TaN and a significant amount of  $\text{Ta}_3\text{N}_6$  phase. After flash sintering, NbN and TiN remain as cubic phase (ICCD-PDF-4 card number 04-004-2895 for NbN and 04-002-1925 for TiN), while the TaN sample converts to a mixture of cubic  $\text{TaN}_{1-x}$  and hexagonal  $\text{TaN}_{0.5}$  phases (ICCD-PDF-4 card number 04-014-0112 and 04-015-0291, respectively). For the three-metal nitrides equimolar mixture sample, after reaction flash sintering, the XRD pattern suggests a single phase with the rock salt structure (like TiN) without any detectable secondary phase or superstructure reflections. The diffraction peaks are narrow, free of shoulders, and the lattice parameter calculated is  $4.33(5)$  Å. Figure 5B shows a zoomed-in section for the (200) peak of the reaction flash sintered three-metal nitrides. The positions for the three individual binary nitrides (assuming cubic phase) are also labeled. The (200) peak for the three-metal nitride is located in between the peaks for the individual nitrides. These results indicate clearly the three binary nitrides form a *complete random solid solution*, presumably  $(\text{Nb}_{1/3}\text{Ta}_{1/3}\text{Ti}_{1/3})\text{N}_{1-\delta}$  after the reaction flash sintering.

Rietveld refinement (see Figure S2) for the  $(\text{Nb}_{1/3}\text{Ta}_{1/3}\text{Ti}_{1/3})\text{N}_{1-\delta}$  random solid solution sample shows a single lattice parameter of  $4.3400(3)$  Å with a nitrogen atom site occupancy value refined as 0.83(2). (The  $R_{\text{wp}}$  value from the GSAS software is 0.0141.) This means in the formula for the three-metal nitride,  $\delta \approx 0.17$ , or  $\sim 17\%$  of nitrogen sites are vacant in the NaCl-structured  $(\text{Nb}_{1/3}\text{Ta}_{1/3}\text{Ti}_{1/3})\text{N}_{1-\delta}$  after the reaction flash sintering.

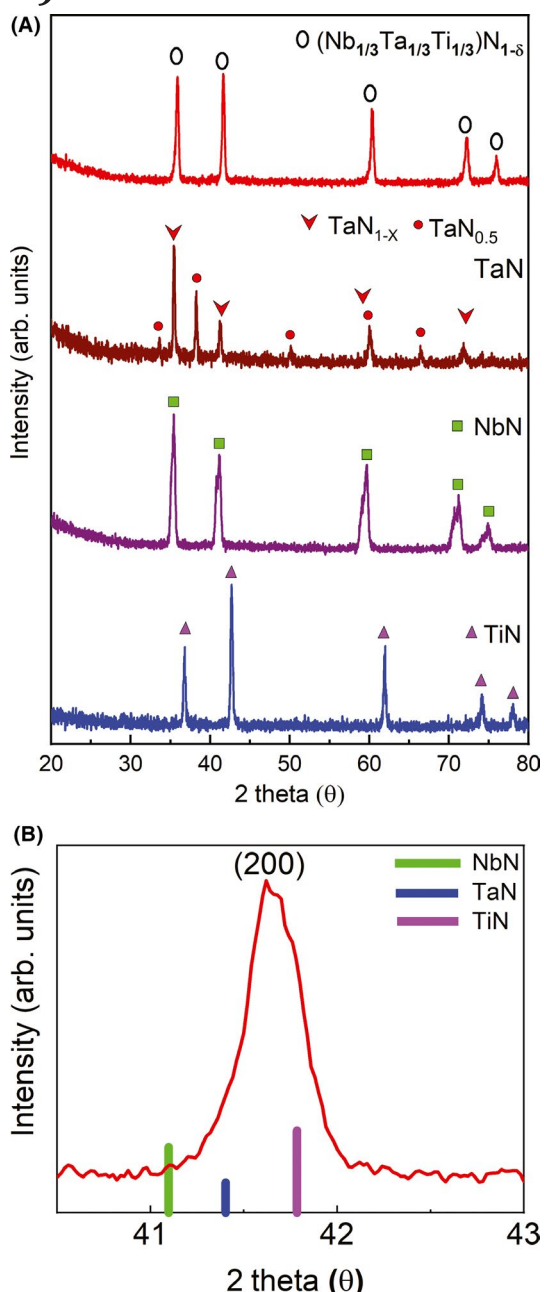


**FIGURE 5** A, XRD patterns of (reaction) flash sintered samples of  $(Nb_{1/3}Ta_{1/3}Ti_{1/3})N_{1-\delta}$  random solid solution from equimolar  $TaN$ ,  $NbN$ , and  $TiN$  mixture, as well as individual  $NbN$ ,  $TaN$ , and  $TiN$ . All samples were ball milled for 2 h and then (reaction) flash sintered with the same limiting current  $I_{lim}$  of 190 A. B, Zoom-in for the (200) diffraction peak of reaction flash sintered  $(Nb_{1/3}Ta_{1/3}Ti_{1/3})N_{1-\delta}$  with the positions for the three ingredient binary cubic nitrides also labeled [Color figure can be viewed at [wileyonlinelibrary.com](http://wileyonlinelibrary.com)]

On the other hand, as will be shown later, the results of the refinement for nitrogen vacancies are in good agreement with that obtained by thermogravimetric (TGA) oxidation experiment.

According to the Ta–N phase diagram,<sup>60</sup> below  $\sim 1750^\circ\text{C}$ , the most stable form of near stoichiometric  $TaN$  is hexagonal, while above  $2000^\circ\text{C}$ , the cubic phase is more stable; in

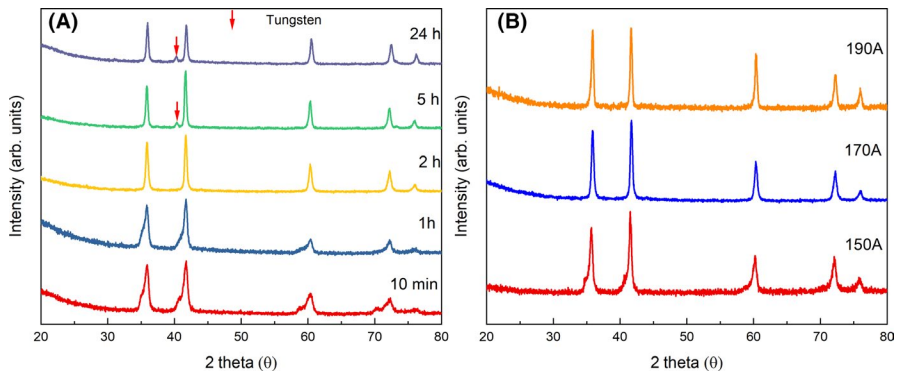
between, mixed phases of cubic and hexagonal might appear depending on temperature and the exact stoichiometry. In comparison, the stable crystal structure of  $TiN^{61}$  and  $NbN^{62}$  are cubic within a larger composition/temperature range. The observation of the three-metal nitride of  $(Nb_{1/3}Ta_{1/3}Ti_{1/3})N_{1-\delta}$  taking the cubic NaCl structure indicates the stabilization for the Ta component, possibly from the combined effects of both enthalpy and entropy stabilization, as discussed later.

### 3.4 | Influence of ball milling time and limiting current on single phase $(Nb_{1/3}Ta_{1/3}Ti_{1/3})N_{1-\delta}$ formation

In this study, the influences of processing parameters such as ball milling time and limiting current are also studied. In particular, Figure 6A shows XRD patterns for the three nitride equimolar mixture samples after different times of ball milling (10 minutes, 1 hour, 2 hours, 5 hours, and 24 hours) followed by reaction flash sintering with initial DC voltage of 8 V and a limiting current  $I_{lim}$  of 170 A (current density of  $\sim 22.5 \text{ A/mm}^2$ ) and hold at  $I_{lim}$  for 120 seconds. The results show that 2 hours of ball milling seems optimal: shorter milling time such as 10 minutes and 1 hour leads to asymmetry in XRD peaks indicating incomplete solid solution formation, while longer milling time such as 5 hours and 24 hours leads to contamination, as evidenced by the minor diffraction peak corresponding to metallic tungsten (red arrow in Figure 6A), which originated from the WC grinding media used. Therefore, 2 hours of ball milling time was selected for subsequent experiments in this work.

The effect of limiting current  $I_{lim}$  on the formation of single phase  $(Nb_{1/3}Ta_{1/3}Ti_{1/3})N_{1-\delta}$  solid solution was also studied. For this, the  $NbN$ - $TaN$ - $TiN$  equimolar mixture was first ball milled for 2 hours and then reaction flash sintered under a constant voltage of 8 V with different limiting currents. Figure 6B shows the XRD patterns of the post reaction flash sintering samples with  $I_{lim}$  of 150, 170, and 190 A and constant hold of 120 seconds at  $I_{lim}$ . When  $I_{lim} = 150 \text{ A}$  (current density of  $19.9 \text{ A/mm}^2$ ), XRD peaks are wide and have shoulders, indicating solid solution formation was not yet complete. When  $I_{lim} = 170 \text{ A}$  (or  $22.5 \text{ A/mm}^2$ ), XRD peaks become narrower and the peak shoulders disappear, which signifies that a complete single phase solid solution is formed. When  $I_{lim}$  further increases to 190 A (or  $25.2 \text{ A/mm}^2$ ), the XRD peaks become even narrower: For example, the full width at half maximum (FWHM) of the (111) peak decreases from  $0.42^\circ$  for the 170 A sample to  $0.36^\circ$  for the 190 A sample, suggesting further grain growth at a higher sintering current. Naturally, higher limiting current leads to higher sintering temperature, which facilitates the formation of complete solid solution. As will be discussed later, higher limiting current also promotes greater densification. Because of all these, a limiting current of 190 A is used

**FIGURE 6** XRD patterns of flash sintered  $(Nb_{1/3}Ta_{1/3}Ti_{1/3})N_{1-\delta}$  samples with (A) different ball milling times but the same limiting current  $I_{lim}$  of 170 A and (B) the same ball milling time of 2 h but different limiting current  $I_{lim}$  of 150, 170, or 190 A [Color figure can be viewed at wileyonlinelibrary.com]



for the rest of the work. (Note that although the maximum current output for the HP 6671A power supply is 220 A, current higher than 190 A ( $25.2 \text{ A/mm}^2$ ) was not explored in order to avoid excessive degradation of the sample assembly—it is currently exposed to air and would experience oxidation in the (reaction) flash sintering experiments. See Figure 1D).

### 3.5 | Microstructure and composition homogeneity for (reaction) flash sintered samples

SEM images of the polished surfaces for reaction flash sintered  $(Nb_{1/3}Ta_{1/3}Ti_{1/3})N_{1-\delta}$  with different limiting current of 170 A ( $22.5 \text{ A/mm}^2$ ) and 190 A ( $25.2 \text{ A/mm}^2$ ) are shown in Figure 7A,B. Naturally, densification improves with higher current (density), as evidenced by reduced pore size and frequency in the 190 A sample versus the 170 A sample.

Figure 7C,D show SEM images of fractured surfaces for the sample sintered at 190 A. The sample appears dense, but there seems to be nonuniformity in the sample's microstructure: large grains of  $\sim 10\text{-}20 \mu\text{m}$  are observed near the surface of the sample (see Figure 7D), whereas the core contains smaller grains of  $\sim 2\text{-}5 \mu\text{m}$  (see Figure 7C). EDS on polished surface of the reaction flash sintered  $(Nb_{1/3}Ta_{1/3}Ti_{1/3})N_{1-\delta}$  sample reveals no indication of elemental clustering at the micron level, as shown in Figure 7E-H.

To compare with the three-metal nitride  $(Nb_{1/3}Ta_{1/3}Ti_{1/3})N_{1-\delta}$ , SEM images of the fractured surfaces of similarly flash sintered NbN, TaN, and TiN samples (all with limiting current of 190 A) are shown in Figure 8. Both NbN (Figure 8A) and TaN (Figure 8B) reveal very dense microstructure with grains larger than  $\sim 20 \mu\text{m}$ . The fractured surface of TiN (Figure 8C) also appears dense but with much smaller  $\sim 2\text{-}5 \mu\text{m}$  grains.

The observation of larger grains near the sample surface and smaller grains at the sample core suggests surface conduction effect, ie, the current density at the surface of the nitride sample might well be larger than the core during the (reaction) flash sintering. However, due to experimental limitation, we could not measure what fraction of current passes from the

sample surface versus from the core. The current modeling as discussed also did not take such surface conduction effect into account. In addition, it is realized that the grain size of the flash sintered  $(Nb_{1/3}Ta_{1/3}Ti_{1/3})N_{1-\delta}$  (with 120 seconds of hold at the limiting current 190 A) near the surface is rather large. This might be due to the fact that the reaction flash sintering process has not been optimized, meaning the grain size might be *smaller with shorter soaking or hold time*. Therefore, measuring and modeling the surface conduction effect for the three nitride powder mixture and more systematic study on the effect of hold time during reaction flash sintering on grain growth will be among the directions for our future research.

### 3.6 | Properties of reaction flash sintered $(Nb_{1/3}Ta_{1/3}Ti_{1/3})N_{1-\delta}$

Measurement of hardness and characterization of the oxidation resistance were conducted on the reaction flash sintered  $(Nb_{1/3}Ta_{1/3}Ti_{1/3})N_{1-\delta}$  and compared with similarly flash sintered NbN, TaN, and TiN as well as literature. The results are presented and discussed here.

#### 3.6.1 | Hardness and comparison with first principle calculation

Measured Vickers hardness of the reaction flash sintered  $(Nb_{1/3}Ta_{1/3}Ti_{1/3})N_{1-\delta}$  as well as the three individual binary nitrides are shown in Figure 9. The average hardness for  $(Nb_{1/3}Ta_{1/3}Ti_{1/3})N_{1-\delta}$  is  $17.6 \pm 0.6 \text{ GPa}$ , which is comparable to the hardness measured for similarly flash sintered NbN ( $17.0 \pm 0.5 \text{ GPa}$ ) and TaN ( $19.0 \pm 1.9 \text{ GPa}$ ) but significantly higher than flash sintered TiN ( $13.2 \pm 0.4 \text{ GPa}$ ). The measured Vickers hardness of the three flash sintered binary nitrides are consistent with previously reported values: ie,  $\sim 13\text{-}35 \text{ GPa}$  for NbN<sup>63-66</sup> and TaN<sup>67-69</sup> and  $\sim 12\text{-}25 \text{ GPa}$  for TiN,<sup>70-73</sup> considering the variations in the types of samples (eg, thin film or bulk material) and the synthesis processes.

As stated before, in order to provide some theoretical insight about the three-metal nitride (solid solution), first

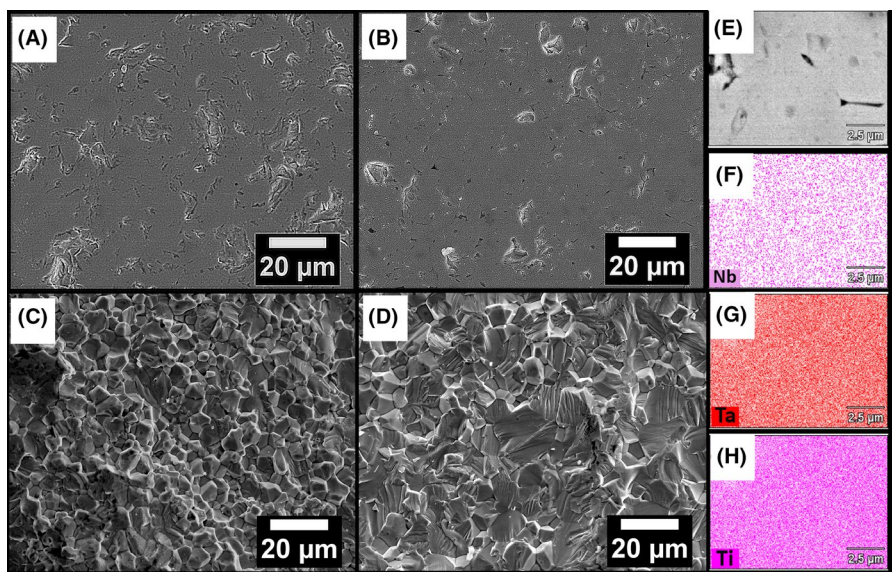


**FIGURE 7** SEM micrographs (A-D) and EDS elemental maps (E-H) for the three-metal nitride  $(Nb_{1/3}Ta_{1/3}Ti_{1/3})N_{1-\delta}$  after reaction flash sintering: (A) and (B) are for the polished surfaces of the samples obtained with limiting current  $I_{lim}$  of 170 A (or 22.5 A/mm<sup>2</sup>) (A) and 190 A (or 25.2 A/mm<sup>2</sup>) (B), respectively; (C) and (D) are for the fractured surfaces of a sample with  $I_{lim}$  of 190 A showing nonuniformity with region of smaller grains in the sample core (C) and region of larger grains near the sample surface (D); (E)-(H) are SEM and corresponding EDS elemental maps from polished surface for a sample with  $I_{lim}$  of 190 A [Color figure can be viewed at wileyonlinelibrary.com]

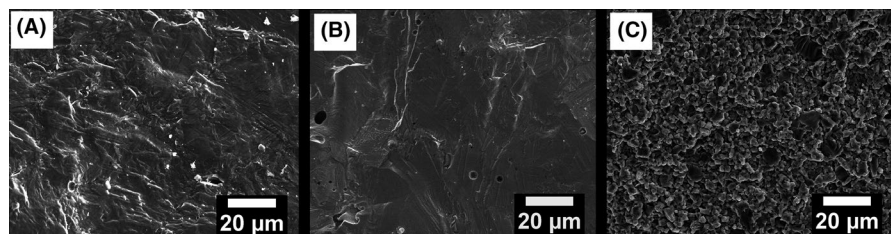


**FIGURE 8** SEM images for fractured surfaces of flash sintered (A) NbN, (B) TaN, and (C) TiN samples. For all three samples, the limiting current  $I_{lim}$  is the same of 190 A (or 25.2 A/mm<sup>2</sup>)

principle calculation has also been carried out in this study. The calculated unit cell volumes of  $(Nb_{1/3}Ta_{1/3}Ti_{1/3})N_{1-\delta}$  as well as the three individual binary nitrides and the corresponding total energy per formula unit are given in Table S2 of the supporting document. The unit cell volume values are in good agreement with the previous experimental and theoretical results.

The mixing enthalpy  $\Delta H_{mix}$  is defined as usual:

$$\Delta H_{mix} = E((Nb_{1/3}Ta_{1/3}Ti_{1/3})N_{1-\delta}) - 1/3E(NbN) - 1/3E(TaN) - 1/3E(TiN),$$

where  $E((Nb_{1/3}Ta_{1/3}Ti_{1/3})N_{1-\delta})$ ,  $E(NbN)$ ,  $E(TaN)$  and  $E(TiN)$  denote, respectively, the calculated relaxed total energies per formula unit for the  $(Nb_{1/3}Ta_{1/3}Ti_{1/3})N_{1-\delta}$  random solid solution and the three individual binary nitrides, respectively.  $\Delta H_{mix}$  was calculated to be  $-6.02$  kJ/mol. A negative enthalpy of mixing together with increased entropy due to mixing naturally favors the thermodynamic stability of the single phase  $(Nb_{1/3}Ta_{1/3}Ti_{1/3})N_{1-\delta}$  random solid solution with respect to the individual binary nitrides.

Calculated bulk modulus ( $B$ ), Young's modulus ( $E$ ), and shear modulus ( $G$ ) of the three individual binary nitrides

and their equimolar random solid solution  $Nb_{1/3}Ta_{1/3}Ti_{1/3})N_{1-\delta}$  are plotted in Figure 10 together with values reported in the literature (both experimental and theoretical, if available). Note that mechanical properties of cubic TiN and NbN are well studied and many data points are available. However, for cubic TaN, which is normally stable only above 1800 K or as a thin film at ambient temperature, very limited experimental results are available.<sup>67-69</sup> Nevertheless, as seen in Figure 10, despite large scattering of the elastic moduli from different sources, both  $G$  and  $E$  seem to decrease with increasing atomic number from Ti to Nb to Ta, while  $B$  shows the opposite trend. The calculated elastic moduli for  $(Nb_{1/3}Ta_{1/3}Ti_{1/3})N_{1-\delta}$  is close to NbN and also the average values calculated by the simple rule of mixture.

With the calculated moduli values, theoretical Vickers hardness was calculated by using the Chen's model,<sup>74</sup> which gives  $H_v = 2(\kappa^2 G)^{0.585} - 3$ , where  $\kappa$  is the Pugh ratio defined as  $\kappa = G/B$ . Figure 11 compares the calculated and experimental Vickers hardness for the three individual binary nitride as well as  $(Nb_{1/3}Ta_{1/3}Ti_{1/3})N_{1-\delta}$ . Data from the literature, both experimental and calculated if available, are also

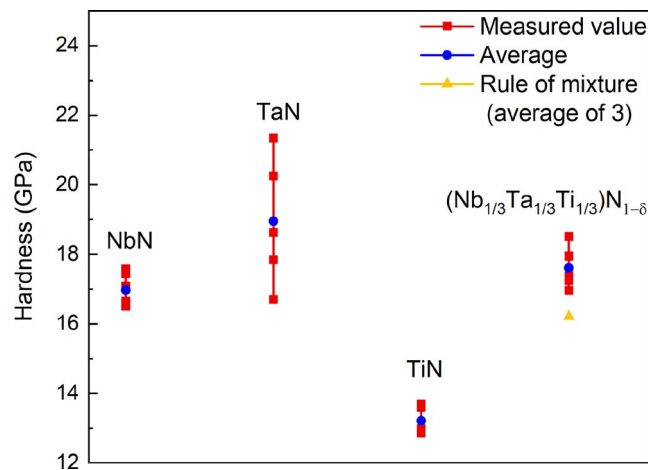


**FIGURE 9** Comparison of measured Vickers hardness of reaction flash sintered  $(\text{Nb}_{1/3}\text{Ta}_{1/3}\text{Ti}_{1/3})\text{N}_{1-\delta}$  vs similarly flash sintered three individual binary nitrides of NbN, TaN, and TiN. For all samples,  $I_{\text{lim}}$  is 190 A (25.2 A/mm<sup>2</sup>) [Color figure can be viewed at wileyonlinelibrary.com]

shown for comparison. The hardness values measured in this study are significantly higher than the predicted values for  $(\text{Nb}_{1/3}\text{Ta}_{1/3}\text{Ti}_{1/3})\text{N}_{1-\delta}$  as well as NbN and TaN. On the other hand, the measured hardness for flash sintered TiN is much lower than both the predicted value from first principle calculation and also literature data.

The reason for the lower measured TiN hardness than predicted is attributed to the lower relative density (~88%, see Table 1) for the flash sintered TiN sample. Such an explanation is also consistent with the observed higher porosity for TiN compared to other samples, as shown in Figure 8. The reason for the higher measured hardness than prediction for the (reaction) flash sintered  $(\text{Nb}_{1/3}\text{Ta}_{1/3}\text{Ti}_{1/3})\text{N}_{1-\delta}$  as well as TaN and NbN might be related to the intrinsic uncertainty in the DFT calculation. Another hypothesis for the higher measured hardness is that it might be due to the nitrogen deficiency in the (reaction) flash sintered samples: Point defects such as vacancies are reported to help pin down dislocations generated during the indentation and increase the hardness. As discussed before, Rietveld analysis shows that  $(\text{Nb}_{1/3}\text{Ta}_{1/3}\text{Ti}_{1/3})\text{N}_{1-\delta}$  seems to have nitrogen deficiency of ~17%. In addition, weight gain in the oxidation tests (to be discussed in the next section) for TaN and NbN also seems to suggest some nitrogen deficiency after flash sintering. More research will be needed in future to provide further verification and understanding of such gaps.

### 3.6.2 | Oxidation resistance

TGA from room temperature to 1300°C in air for pieces broken off from (reaction) flash sintered  $(\text{Nb}_{1/3}\text{Ta}_{1/3}\text{Ti}_{1/3})\text{N}_{1-\delta}$  as well as the three individual binary nitride samples are plotted in Figure 12. Qualitatively, the oxidation resistance

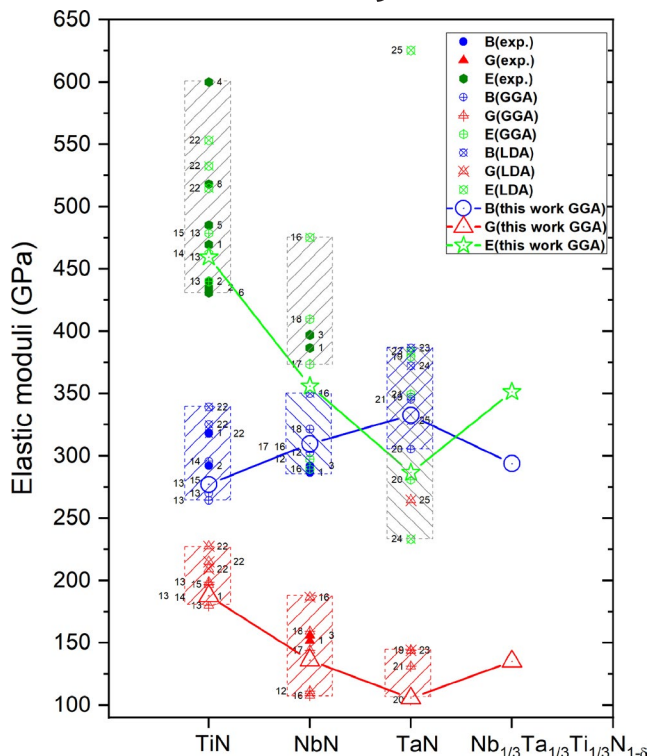


**FIGURE 10** Calculated elastic moduli (bulk modulus  $B$ , Young's modulus  $E$ , and shear modulus  $G$ ) for NbN, TaN, and TiN, as well as  $(\text{Nb}_{1/3}\text{Ta}_{1/3}\text{Ti}_{1/3})\text{N}_{1-\delta}$ . Reported experimental and calculated values for the three binary nitrides in the literature are also shown for comparison. The numbered points in the graph are referring to different references as below: 1-8 are from Ref. [84-91], 9 from Ref. [71], 10-11 from Ref. [63,64], 12-25 from Ref. [92-104], 26 from Ref. [68], and 27 from Ref. [67]. Note that nano-indentation measurement in this study on  $(\text{Nb}_{1/3}\text{Ta}_{1/3}\text{Ti}_{1/3})\text{N}_{1-\delta}$  gives reduced Young's modulus  $E_r$  of 318 GPa. Assuming Poisson ratio  $\nu$  for  $(\text{Nb}_{1/3}\text{Ta}_{1/3}\text{Ti}_{1/3})\text{N}_{1-\delta}$  is 0.30,  $E$  is estimated to be ~349 GPa, which is close to the predicted value [Color figure can be viewed at wileyonlinelibrary.com]

of  $(\text{Nb}_{1/3}\text{Ta}_{1/3}\text{Ti}_{1/3})\text{N}_{1-\delta}$  random solid solution is better than TaN and NbN, as evidenced by the higher onset temperature for weight gain in air: ~850°C for  $(\text{Nb}_{1/3}\text{Ta}_{1/3}\text{Ti}_{1/3})\text{N}_{1-\delta}$  vs ~750°C for TaN and ~600°C for NbN. When compared with TiN, below ~850°C,  $(\text{Nb}_{1/3}\text{Ta}_{1/3}\text{Ti}_{1/3})\text{N}_{1-\delta}$  behaves similar to TiN. Above 850°C, the oxidation resistance of TiN appears better than  $(\text{Nb}_{1/3}\text{Ta}_{1/3}\text{Ti}_{1/3})\text{N}_{1-\delta}$ , as evidenced by TiN's higher onset oxidation temperature (~1100°C) and also lower relative weight gain.

The measured maximum weight gain during TGA in air for sintered NbN is 25.8% after the sample weight reaches plateau. This is slightly *higher* than the expected value of ~24.3% for complete oxidation of stoichiometric NbN to  $\text{Nb}_2\text{O}_5$  and  $\text{N}_2$ . In fact, based on the measured weight gain value, the flash sintered sample should have a nominal composition of NbN<sub>0.91</sub>, which is reasonable given the possibility of nitrogen deficiency in the Nb-N system and the high temperature reached during flash sintering.

For TaN, the measured peak weight gain (at  $\sim 1150^{\circ}\text{C}$ ) is 19.5%. This is much *higher* than the expected value of  $\sim 13.3\%$  for complete oxidation of stoichiometric TaN to  $\text{Ta}_2\text{O}_5$  and  $\text{N}_2$ .<sup>75,76</sup> (Under such assumption of complete nitrogen release, the 19.5% weight gain would indicate a very large nitrogen deficiency of  $\sim 70\%$  in the flash sintered TaN, which appears too low considering XRD analysis of the

flash sintered TaN showing it is actually a mixture of  $\text{TaN}_{0.5}$  and TaN, see Figure 5A). Nevertheless, flash sintered  $\text{TaN}_x$  shows multi-stage oxidation: In the first stage oxidation at lower temperature up to  $\sim 850^{\circ}\text{C}$ , the product might be  $\text{TaON}_x$  without release of any gaseous compound.<sup>77</sup> Upon further increase in temperature to  $\sim 1000^{\circ}\text{C}$  and above,  $\text{TaON}_x$  oxidizes further and eventually converts to  $\text{Ta}_2\text{O}_5$ , which is confirmed by XRD (see discussion later). In terms of morphology, both NbN and TaN oxidation products look like agglomerated loose powders. This is attributed to the large volume expansion in the conversion from nitrides to oxides.

In comparison, the weight gain in TGA oxidation of flash sintered TiN is only  $\sim 6\%$  at  $1300^{\circ}\text{C}$ , which is much *lower* than the calculated value of  $\sim 29.1\%$  for complete TiN conversion to  $\text{TiO}_2$  or the value of 25.8% for TiN conversion to  $\text{TiON}$ . This indicates the oxidation of flash sintered TiN is rather slow. After the TGA oxidation of TiN up to  $1300^{\circ}\text{C}$ , the oxide layer appears as a dense, continuous coating over the bulk remaining TiN, as shown in Figure 12B, which is expected to reduce the oxidation rate.

The TGA oxidation of the  $(\text{Nb}_{1/3}\text{Ta}_{1/3}\text{Ti}_{1/3})\text{N}_{1-\delta}$  solid solution results in a total weight gain of  $\sim 12.5\%$  at  $1300^{\circ}\text{C}$ . The expected weight gain for complete oxidation of  $(\text{Nb}_{1/3}\text{Ta}_{1/3}\text{Ti}_{1/3})\text{N}_{1-\delta}$  to individual binary oxides (ie,  $\text{Nb}_2\text{O}_5$ ,  $\text{Ta}_2\text{O}_5$ , and  $\text{TiO}_2$ ) is 22.2%. The lower than expected weight gain signifies improved oxidation resistance for  $(\text{Nb}_{1/3}\text{Ta}_{1/3}\text{Ti}_{1/3})\text{N}_{1-\delta}$  over NbN and TaN, but still not as good as TiN. The SEM image of the surface of  $(\text{Nb}_{1/3}\text{Ta}_{1/3}\text{Ti}_{1/3})\text{N}_{1-\delta}$  after TGA oxidation (see Figure 12C) shows a fine grainy structure, which appears not as smooth and dense as the coating over oxidized TiN.

XRD shows that the oxidation products of flash sintered TaN and NbN are  $\text{Ta}_2\text{O}_5$  and  $\text{Nb}_2\text{O}_5$ , respectively (Figure 13B,C), which has melting temperature of 1872 and  $1512^{\circ}\text{C}$ , respectively.<sup>78-80</sup> Whereas  $(\text{Nb}_{1/3}\text{Ta}_{1/3}\text{Ti}_{1/3})\text{N}_{1-\delta}$ , upon TGA oxidation (Figure 13A), yields  $\text{Ti}(\text{NbTa})\text{O}_7$ , the solid solution between  $\text{TiNb}_2\text{O}_7$  (ICCD-PDF-4 no. 00-039-1407, melting temperature  $1497^{\circ}\text{C}$ ) and  $\text{TiTa}_2\text{O}_7$  (ICCD-PDF-4 no.

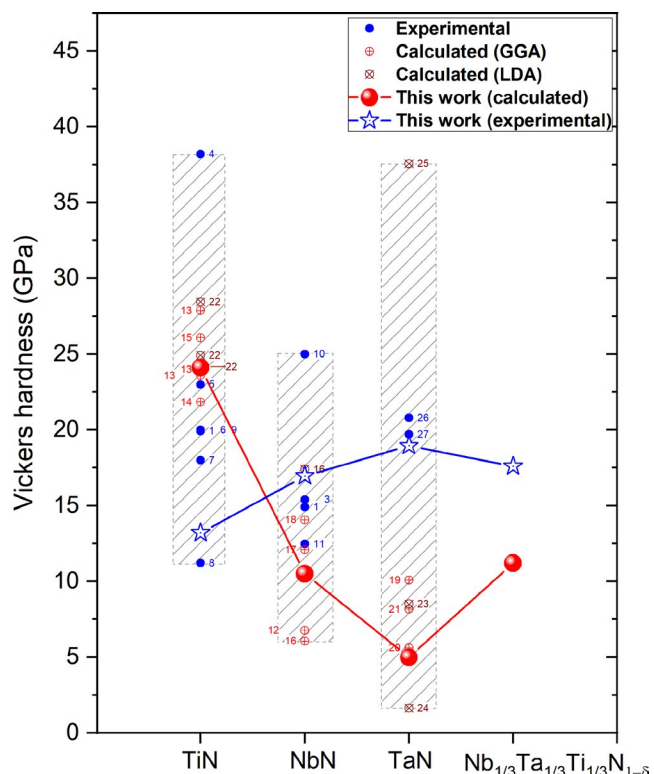


**FIGURE 11** Experimental and calculated Vickers hardness of NbN, TaN, and TiN, as well as  $(\text{Nb}_{1/3}\text{Ta}_{1/3}\text{Ti}_{1/3})\text{N}_{1-\delta}$ . Literature reported hardness values, if available, are also shown for comparison. The points in the graph referred as 1-8 are from Ref. [84-91], 9 from Ref. [71], 10-11 from Ref. [63,64], 12-25 from Ref. [92-104], 26 from Ref. [68], and 27 from Ref. [67] [Color figure can be viewed at wileyonlinelibrary.com]

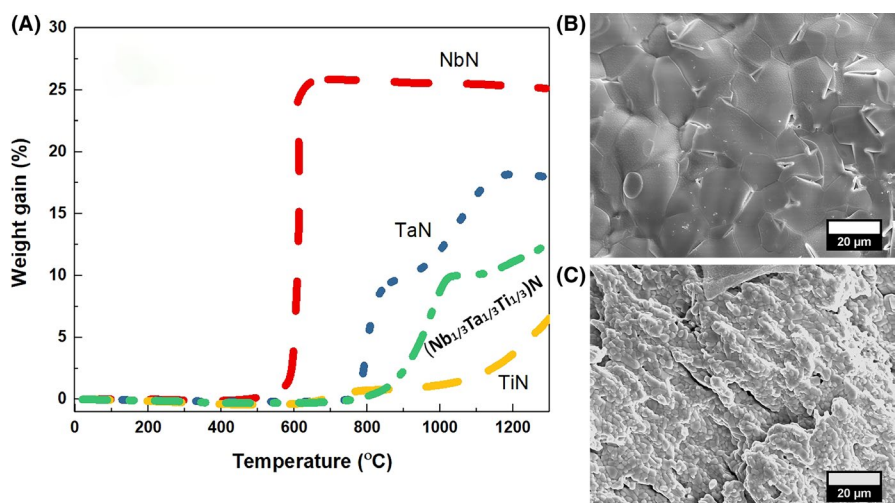


**FIGURE 12** A, TGA in air from room temperature to  $1300^{\circ}\text{C}$  for fractured pieces from (reaction) flash sintered  $(\text{Nb}_{1/3}\text{Ta}_{1/3}\text{Ti}_{1/3})\text{N}_{1-\delta}$ , NbN, TaN, and TiN samples. B and C, are SEM images of the surface for TiN (B) and  $(\text{Nb}_{1/3}\text{Ta}_{1/3}\text{Ti}_{1/3})\text{N}_{1-\delta}$  (C) after TGA oxidation [Color figure can be viewed at wileyonlinelibrary.com]

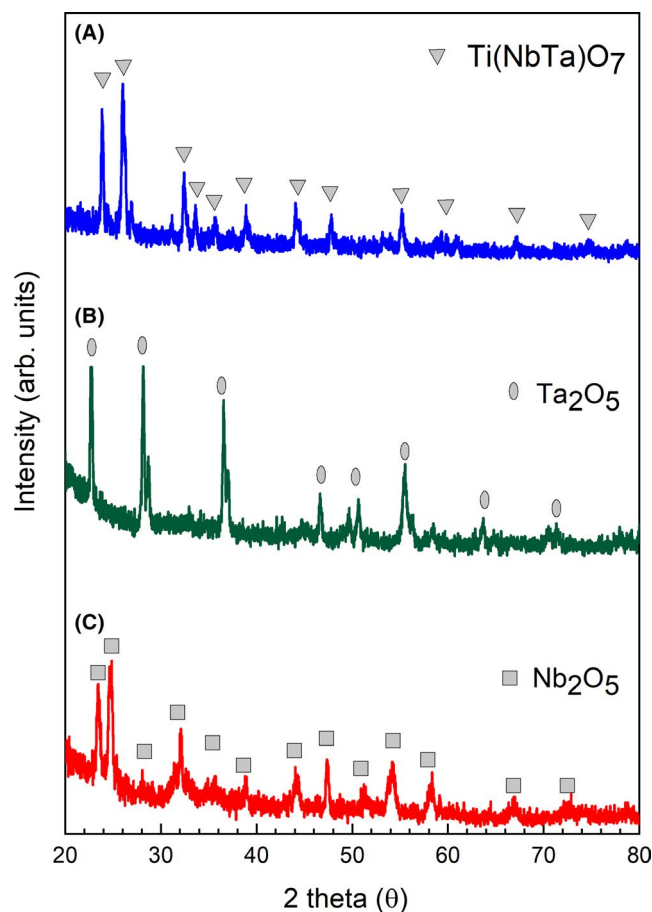


**FIGURE 13** XRD patterns for oxidation products (1300°C TGA in air) for (reaction) flash sintered (A)  $(\text{Nb}_{1/3}\text{Ta}_{1/3}\text{Ti}_{1/3})\text{N}_{1-\delta}$ , (B) TaN, and (C) NbN. After oxidation,  $(\text{Nb}_{1/3}\text{Ta}_{1/3}\text{Ti}_{1/3})\text{N}_{1-\delta}$  turned into complex Ti-Ta-Nb oxide(s) ( $\text{Ti}(\text{NbTa})\text{O}_7$ ), TaN turned into  $\text{Ta}_2\text{O}_5$ , and NbN turned into  $\text{Nb}_2\text{O}_5$  [Color figure can be viewed at wileyonlinelibrary.com]

01-084-8891, melting temperature 1661°C.<sup>81-83</sup> Whether the lowered melting point for the oxidation products from  $(\text{Nb}_{1/3}\text{Ta}_{1/3}\text{Ti}_{1/3})\text{N}_{1-\delta}$  or other effects helped improve the oxidation resistance for  $(\text{Nb}_{1/3}\text{Ta}_{1/3}\text{Ti}_{1/3})\text{N}_{1-\delta}$  over binary nitrides of NbN or TaN needs to be studied in future.

## 4 | CONCLUSIONS

In conclusion, a new bulk single phase three-metal nitride of  $(\text{Nb}_{1/3}\text{Ta}_{1/3}\text{Ti}_{1/3})\text{N}_{1-\delta}$  has been successfully synthesized through reaction flash sintering from a ball milled equimolar mixture of commercial NbN, TaN, and TiN powders. Reaction flash sintering was carried out at 25°C under applied pressure of ~35 MPa and low initial DC electrical field (~24 to 32 V/cm). Without preheating, flash occurred with quick increase of current density up to ~ 25.2 A/mm<sup>2</sup>. The samples' effective resistance dropped by 600 times or more in the process, while the threshold power dissipation right before the flash event was ~0.7 W/mm<sup>3</sup> and increased up to ~50 W/mm<sup>3</sup> when

reaching the steady state. XRD shows that the product takes the cubic rock salt structure, while SEM and EDS show that the product has relative density above 99% and uniformity in distribution of elements.  $(\text{Nb}_{1/3}\text{Ta}_{1/3}\text{Ti}_{1/3})\text{N}_{1-\delta}$  gives hardness comparable to similarly flash sintered binary nitrides such as NbN and TaN. Oxidation resistance of  $(\text{Nb}_{1/3}\text{Ta}_{1/3}\text{Ti}_{1/3})\text{N}_{1-\delta}$ , in terms of TGA weight gain and onset temperature, is better than TaN and NbN, but not as good as TiN. The study may also serve as the foundation for use of reaction flash sintering for the development of other multicomponent (including high entropy) ceramics in future. Future study in both experiments and theoretical modeling are required for better control and understanding of the reaction flash sintering process and properties of the resulting materials, including investigation of the effect of surface conduction, determination of sample nitrogen deficiency with greater confidence, and process optimization for reduced heat loss, higher energy efficiency, and finer grain structure, etc.

## ACKNOWLEDGMENTS

Authors ZC and JB acknowledge the support from the DOE National Energy Technology Laboratory (NETL) Crosscutting Research Program grant number DE-FE0026325. Dr Logesh Mathivathanan helped with the X-ray diffraction study. The authors also acknowledge National Supercomputer Center in Sweden (NSC) for providing the computing resources.

## ORCID

Santanu Mondal  <https://orcid.org/0000-0002-3572-3036>  
Zhe Cheng  <https://orcid.org/0000-0002-7332-604X>

## REFERENCES

- Koseki S, Inoue K, Morito S, Ohba T, Usuki H. Comparison of TiN-coated tools using CVD and PVD processes during continuous cutting of Ni-based superalloys. *Surf Coat Technol*. 2015;283:353–63. <https://doi.org/10.1016/j.surfcoat.2015.10.071>
- Hones P, Diserens M, Sanjinés R, Lévy F. Electronic structure and mechanical properties of hard coatings from the chromium-tungsten nitride system. *J Vac Sci Technol B: Microelectronics and Nanometer Structures*. 2000;18(6):2851–6. <https://doi.org/10.1116/1.1320806>
- Polcar T, Cavaleiro A. Structure, mechanical properties and tribology of W-N and W-O coatings. *Int J Refract Hard Met*. 2010;28(1):15–22. <https://doi.org/10.1016/j.ijrmhm.2009.07.013>
- Zhang K, Balasubramanian K, Ozsdolay BD, Mulligan CP, Khare SV, Zheng WT, et al. Epitaxial NbCxN1-x(001) layers: growth, mechanical properties, and electrical resistivity. *Surf Coat Technol*. 2015;277:136–43.
- Musil J. Hard and superhard nanocomposite coatings. *Surf Coat Technol*. 2000;125(1–3):322–30. [https://doi.org/10.1016/S0257-8972\(99\)00586-1](https://doi.org/10.1016/S0257-8972(99)00586-1)
- Wittmer M. TiN and TaN as diffusion barriers in metallizations to silicon semiconductor devices. *Appl Phys Lett*. 1980;36(6):456–8. <https://doi.org/10.1063/1.91505>

7. Oku T, Kawakami E, Uekubo M, Takahiro K, Yamaguchi S, Murakami M. Diffusion barrier property of TaN between Si and Cu. *Appl Surf Sci.* 1996;99(4):265–72. [https://doi.org/10.1016/0169-4332\(96\)00464-3](https://doi.org/10.1016/0169-4332(96)00464-3)
8. Min KH, Chun KC, Kim KB. Comparative study of tantalum and tantalum nitrides (Ta<sub>2</sub>N and TaN) as a diffusion barrier for Cu metallization. *J Vac Sci Technol B.* 1996;14(5):3263–9. <https://doi.org/10.1116/1.588818>
9. Wuchina E, Opila E, Opeka M, Fahrenholtz W, Talmy I. UHTCs: ultra-high temperature ceramic materials for extreme environment applications. *Electrochem Soc Interface.* 2007;16(4):30.
10. Gregoryanz E, Sanloup C, Somayazulu M, Badro J, Fiquet G, Mao H-K, et al. Synthesis and characterization of a binary noble metal nitride. *Nat Mater.* 2004;3(5):294–7. <https://doi.org/10.1038/nmat1115>
11. Zhong Y, Xia X, Shi F, Zhan J, Tu J, Fan HJ. Transition Metal Carbides and Nitrides in Energy Storage and Conversion. *Adv Sci.* 2016;3(5):1500286. <https://doi.org/10.1002/advs.201500286>
12. Balasubramanian K, Khare SV, Gall D. Energetics of point defects in rocksalt structure transition metal nitrides: thermodynamic reasons for deviations from stoichiometry. *Acta Mater.* 2018;159:77–88. <https://doi.org/10.1016/j.actamat.2018.07.074>
13. Wen Z, Cui S, Pu H, Mao S, Yu K, Feng X, et al. Metal nitride/graphene nanohybrids: general synthesis and multifunctional titanium nitride/graphene electrocatalyst. *Adv Mater (Deerfield Beach, Fla).* 2011;23(45):5445–50. <https://doi.org/10.1002/adma.201102772>
14. Toth L. Transition metal carbides and nitrides. New York, NY: Academic Press; 1971.
15. Shen WJ, Tsai MH, Tsai KY, Juan CC, Tsai CW, Yeh JW, et al. Superior oxidation resistance of (Al<sub>0.34</sub>Cr<sub>0.22</sub>Nb<sub>0.11</sub>Si<sub>0.11</sub>Ti<sub>0.22</sub>)<sub>50</sub>N<sub>50</sub> high-entropy nitride. *J Electrochem Soc.* 2013;160(11):C53–C55. <https://doi.org/10.1149/2.028311jes>
16. Braic M, Braic V, Vladescu A, Balaceanu M, Luculescu CR. Nanostructured multi-element (TiZrNbHfTa)N and (TiZrNbHfTa) C hard coatings. *Surf Coat Technol.* 2012;211:117–21. <https://doi.org/10.1016/j.surfcoat.2011.09.033>
17. Robbins SW, Sai H, DiSalvo FJ, Gruner SM, Wiesner U. Monolithic gyroidal mesoporous mixed titanium-niobium nitrides. *ACS Nano.* 2014;8(8):8217–23. <https://doi.org/10.1021/nn502548m>
18. Brancho JJ, Proctor AD, Panuganti S, Bartlett BM. Urea-glass preparation of titanium niobium nitrides and subsequent oxidation to photoactive titanium niobium oxynitrides. *Dalton Trans.* 2017;46(36):12081–7.
19. Gomathi A, Rao CNR. Nanostructures of the binary nitrides, BN, TiN, and NbN, prepared by the urea-route. *Mater Res Bull.* 2006;41(5):941–7. <https://doi.org/10.1016/j.materresbull.2006.01.015>
20. Zakutayev A, Allen AJ, Zhang X, Vidal J, Cui Z, Lany S, et al. Experimental synthesis and properties of metastable CuNbN<sub>2</sub> and theoretical extension to other ternary copper nitrides. *Chem Mater.* 2014;26(17):4970–7. <https://doi.org/10.1021/cm5018135>
21. Luo J, Tian X, Zeng J, Li Y, Song H, Liao S. Limitations and improvement strategies for early-transition-metal nitrides as competitive catalysts toward the oxygen reduction reaction. *ACS Catal.* 2016;6(9):6165–74. <https://doi.org/10.1021/acscatal.6b01618>
22. Sun Q, Fu Z-W. Cr<sub>1-x</sub>Fe<sub>x</sub>N (0≤x≤1) ternary transition-metal nitrides as anode materials for lithium-ion batteries. *Electrochem Solid-State Lett.* 2008;11(12):A233. <https://doi.org/10.1149/1.2988835>
23. Cologna M, Rashkova B, Raj R. Flash sintering of nanograin zirconia in 5 s at 850°C. *J Am Ceram Soc.* 2010;93(11):3556–9. <https://doi.org/10.1111/j.1551-2916.2010.04089.x>
24. Yu M, Grasso S, McKinnon R, Saunders T, Reece MJ. Review of flash sintering: materials, mechanisms and modelling. *Adv Appl Ceram.* 2017;116(1):24–60. <https://doi.org/10.1080/17436753.2016.1251051>
25. Raj R, Cologna M, Francis JSC. Influence of externally imposed and internally generated electrical fields on grain growth, diffusional creep, sintering and related phenomena in ceramics. *J Am Ceram Soc.* 2011;94(7):1941–65. <https://doi.org/10.1111/j.1551-2916.2011.04652.x>
26. Zhang Y, Nie J, Chan JM, Luo J. Probing the densification mechanisms during flash sintering of ZnO. *Acta Mater.* 2017;125:465–75. <https://doi.org/10.1016/j.actamat.2016.12.015>
27. Charalambous H, Jha SK, Lay RT, Cabales A, Okasinski J, Tsakalakos T. Investigation of temperature approximation methods during flash sintering of ZnO. *Ceram Int.* 2018;44(6):6162–9. <https://doi.org/10.1016/j.ceramint.2017.12.250>
28. Zhang Y, Jung J-I, Luo J. Thermal runaway, flash sintering and asymmetrical microstructural development of ZnO and ZnO–Bi<sub>2</sub>O<sub>3</sub> under direct currents. *Acta Mater.* 2015;94:87–100. <https://doi.org/10.1016/j.actamat.2015.04.018>
29. Jesus LM, Silva RS, Raj R, M'Peko J-C. Electric field-assisted flash sintering of CaCu<sub>3</sub>Ti<sub>4</sub>O<sub>12</sub>: microstructure characteristics and dielectric properties. *J Alloys Compd.* 2016;682:753–8. <https://doi.org/10.1016/j.jallcom.2016.05.002>
30. Prette ALG, Cologna M, Sglavo V, Raj R. Flash-sintering of Co<sub>2</sub>MnO<sub>4</sub> spinel for solid oxide fuel cell applications. *J Power Sources.* 2011;196(4):2061–5. <https://doi.org/10.1016/j.jpowsour.2010.10.036>
31. Gaur A, Sglavo VM. Flash-sintering of MnCo<sub>2</sub>O<sub>4</sub> and its relation to phase stability. *J Eur Ceram Soc.* 2014;34(10):2391–400. <https://doi.org/10.1016/j.jeurceramsoc.2014.02.012>
32. Gaur A, Sglavo VM. Sglavo V. Densification of La<sub>0.6</sub>Sr<sub>0.4</sub>Co<sub>0.2</sub>Fe<sub>0.8</sub>O<sub>3</sub> ceramic by flash sintering at temperature less than 100°C. *J Mater Sci.* 2014;49(18):6321–32.
33. Kok D, Jha SK, Raj R, Mecartney ML. Flash sintering of a three-phase alumina, spinel, and yttria-stabilized zirconia composite. *J Am Ceram Soc.* 2017;100(7):3262–8. <https://doi.org/10.1111/jace.14818>
34. Francis JSC, Cologna M, Montinaro D, Raj R, Wei WC. Flash sintering of anode-electrolyte multilayers for SOFC applications. *J Am Ceram Soc.* 2013;96(5):1352–4. <https://doi.org/10.1111/jace.12330>
35. Liu D, Gao Y, Liu J, Liu F, Li K, Su H, et al. Preparation of Al<sub>2</sub>O<sub>3</sub>–Y<sub>3</sub>Al<sub>5</sub>O<sub>12</sub>–ZrO<sub>2</sub> eutectic ceramic by flash sintering. *Scr Mater.* 2016;114:108–11. <https://doi.org/10.1016/j.scriptamat.2015.12.002>
36. Liu D, Gao Y, Liu J, Li K, Liu F, Wang Y, et al. SiC whisker reinforced ZrO<sub>2</sub> composites prepared by flash-sintering. *J Eur Ceram Soc.* 2016;36(8):2051–5. <https://doi.org/10.1016/j.jeurceramsoc.2016.02.014>
37. Luo J. The scientific questions and technological opportunities of flash sintering: from a case study of ZnO to other ceramics. *Scr Mater.* 2018;146:260–6. <https://doi.org/10.1016/j.scriptamat.2017.12.006>

38. Yoon B, Yadav D, Ghose S, Raj R. Reactive flash sintering: MgO and  $\alpha$ -Al<sub>2</sub>O<sub>3</sub> transform and sinter into single-phase polycrystals of MgAl<sub>2</sub>O<sub>4</sub>. *J Am Ceram Soc.* 2019;102(5):2294–303. <https://doi.org/10.1111/jace.15974>
39. Gil-González E, Perejón A, Sánchez-Jiménez PE, Sayagués MJ, Raj R, Pérez-Maqueza LA. Phase-pure BiFeO<sub>3</sub> produced by reaction flash-sintering of Bi<sub>2</sub>O<sub>3</sub> and Fe<sub>2</sub>O<sub>3</sub>. *J Mater Chem A.* 2018;6(13):5356–66. <https://doi.org/10.1039/C7TA09239C>
40. Zunger A, Wei S, Ferreira LG, Bernard JE. Special quasirandom structures. *Phys Rev Lett.* 1990;65(3):353–6. <https://doi.org/10.1103/PhysRevLett.65.353>
41. van de Walle A, Asta M, Ceder G. The alloy theoretic automated toolkit: a user guide. *Calphad.* 2002;26(4):539–53. [https://doi.org/10.1016/S0364-5916\(02\)80006-2](https://doi.org/10.1016/S0364-5916(02)80006-2)
42. Kresse G, Furthmüller J. Efficiency of ab-initio total energy calculations for metals and semiconductors using a plane-wave basis set. *Comput Mater Sci.* 1996;6(1):15–50. [https://doi.org/10.1016/0927-0256\(96\)00008-0](https://doi.org/10.1016/0927-0256(96)00008-0)
43. Kresse G, Furthmüller J. Efficient iterative schemes for ab initio total-energy calculations using a plane-wave basis set. *Phys Rev B Condens Matter.* 1996;54(16):11169–86. <https://doi.org/10.1103/PhysRevB.54.11169>
44. Perdew JP, Chevary JA, Vosko SH, Jackson KA, Pederson MR, Singh DJ, et al. Atoms, molecules, solids, and surfaces: applications of the generalized gradient approximation for exchange and correlation. *Phys Rev B Condens Matter.* 1992;46(11):6671–87. <https://doi.org/10.1103/PhysRevB.46.6671>
45. Perdew JP, Burke K, Ernzerhof M. Generalized gradient approximation made simple. *Phys Rev Lett.* 1996;77(18):3865–8. <https://doi.org/10.1103/PhysRevLett.77.3865>
46. Monkhorst HJ, Pack JD. Special points for Brillouin-zone integrations. *Phys Rev B.* 1976;13(12):5188–92. <https://doi.org/10.1103/PhysRevB.13.5188>
47. Gaillac R, Pullumbi P, Couder F-X. ELATE: an open-source online application for analysis and visualization of elastic tensors. *J Phys: Condens Matter.* 2016;28(27):275201. <https://doi.org/10.1088/0953-8984/28/27/275201>
48. de Jong M, Chen W, Angsten T, Jain A, Notestine R, Gamst A, et al. Charting the complete elastic properties of inorganic crystalline compounds. *Sci Data.* 2015;2(1):150009. <https://doi.org/10.1038/sdata.2015.9>
49. Francis JSC, Raj R, Chen IW. Flash-sinterforging of nanograin zirconia: field assisted sintering and superplasticity. *J Am Ceram Soc.* 2012;95(1):138–46. <https://doi.org/10.1111/j.1551-2916.2011.04855.x>
50. Okada M, Ohta N, Yoshimoto O, Tatsumi M, Inagaki M. Review on the high-temperature resistance of graphite in inert atmospheres. *Carbon.* 2017;116:737–43. <https://doi.org/10.1016/j.carbon.2017.02.039>
51. Raj R, Chan H. Analysis of the power density at the onset of flash sintering. *J Am Ceram Soc.* 2016;99(10):3226–32. <https://doi.org/10.1111/jace.14178>
52. Biesuz M, Sglavo VM. Flash sintering of ceramics. *J Eur Ceram Soc.* 2019;39(2):115–43. <https://doi.org/10.1016/j.jeurceramsoc.2018.08.048>
53. Lal K, Meikap AK, Chattopadhyay SK, Chatterjee SK, Ghosh M, Baba K, et al. Electrical resistivity of titanium nitride thin films prepared by ion beam-assisted deposition. *Physica B Condens Matter.* 2001;307(1):150–7. [https://doi.org/10.1016/S0921-4526\(01\)00626-3](https://doi.org/10.1016/S0921-4526(01)00626-3)
54. Duan G, Zhao G, Wu L, Lin X, Han G. Structure, electrical and optical properties of TiN<sub>x</sub> films by atmospheric pressure chemical vapor deposition. *Appl Surf Sci.* 2011;257(7):2428–31. <https://doi.org/10.1016/j.apsusc.2010.11.180>
55. Nie HB, Xu SY, Wang SJ, You LP, Yang Z, Ong CK, et al. Structural and electrical properties of tantalum nitride thin films fabricated by using reactive radio-frequency magnetron sputtering. *Appl Phys A.* 2001;73(2):229–36. <https://doi.org/10.1007/s003390000691>
56. Kaul AB, Whiteley SR, Van Duzer T, Yu L, Newman N, Rowell JM. Internally shunted sputtered NbN Josephson junctions with a TaNx barrier for nonlatching logic applications. *Appl Phys Lett.* 2000;78(1):99–101. <https://doi.org/10.1063/1.1337630>
57. Nigro A, Nobile G, Rubino MG, Vaglio R. Electrical resistivity of polycrystalline niobium nitride films. *Phys Rev B.* 1988;37(8):3970–2. <https://doi.org/10.1103/PhysRevB.37.3970>
58. Hotovy I, Buc D, Brcka J, Srnanek R. Study of niobium nitride films produced by DC reactive magnetron sputtering. *Phys Status Solidi (a).* 1997;161(1):97–104.
59. Raj R. Joule heating during flash-sintering. *J Eur Ceram Soc.* 2012;32(10):2293–301. <https://doi.org/10.1016/j.jeurceramsoc.2012.02.030>
60. Cheviet M, Gouné M, Poulon-Quintin A. Monitoring tantalum nitride thin film structure by reactive RF magnetron sputtering: influence of processing parameters. *Surf Coat Technol.* 2015;284:192–7. <https://doi.org/10.1016/j.surfcoat.2015.08.075>
61. Wriedt HA, Murray JL. The N-Ti (Nitrogen-Titanium) system. *Bulletin of Alloy Phase Diagrams.* 1987;8(4):378–88. <https://doi.org/10.1007/BF02869274>
62. Huang W. Thermodynamic assessment of the Nb-N system. *Metall Mater Trans A.* 1996;27(11):3591–600. <https://doi.org/10.1007/BF02595450>
63. Ran S, Gao L. Spark plasma sintering of nanocrystalline niobium nitride powders. *J Am Ceram Soc.* 2008;91(2):599–602. <https://doi.org/10.1111/j.1551-2916.2007.02183.x>
64. Sandu CS, Benkahoul M, Parlinska-Wojtan M, Sanjinés R, Lévy F. Morphological, structural and mechanical properties of NbN thin films deposited by reactive magnetron sputtering. *Surf Coat Technol.* 2006;200(22–23):6544–8. <https://doi.org/10.1016/j.surfcoat.2005.11.054>
65. Benkahoul M, Zayed MK, Sandu CS, Martinu L, Klembberg-Sapieha JE. Structural, tribo-mechanical, and thermal properties of NbAlN coatings with various Al contents deposited by DC reactive magnetron sputtering. *Surf Coat Technol.* 2017;331:172–8. <https://doi.org/10.1016/j.surfcoat.2017.10.038>
66. Zhang E, Liu J, Li W. Microstructures, mechanical and tribological properties of NbN/MoS<sub>2</sub> nanomultilayered films deposited by reactive magnetron sputtering. *Vacuum.* 2019;160:205–9. <https://doi.org/10.1016/j.vacuum.2018.11.038>
67. Li R, Qin Y, Liu G, Zhang C, Liang H, Qing Y, et al. Tantalum nitride coatings prepared by magnetron sputtering to improve the bioactivity and osteogenic activity for titanium alloy implants. *RSC Adv.* 2017;7(87):55408–17. <https://doi.org/10.1039/C7RA09032C>
68. Zhang K, Liu C, Wen M, Chen Y, Song J, Yang L, et al. Functional coatings: doping Cu atoms excel as the functional material to tune the wettability for TMeNs hard coating. *Adv Mater Inter.* 2018;5(18):1800391. <https://doi.org/10.1002/admi.201870086>
69. Bernoulli D, Müller U, Schwarzenberger M, Hauert R, Spolenak R. Magnetron sputter deposited tantalum and tantalum nitride thin

- films: An analysis of phase, hardness and composition. *Thin Solid Films*. 2013;548:157–61. <https://doi.org/10.1016/j.tsf.2013.09.055>
70. Cheng H-E, Wen Y-W. Correlation between process parameters, microstructure and hardness of titanium nitride films by chemical vapor deposition. *Surf Coat Technol*. 2004;179(1):103–9. [https://doi.org/10.1016/S0257-8972\(03\)00789-8](https://doi.org/10.1016/S0257-8972(03)00789-8)
71. Kolesnichenko VG, Popov VP, Zgalat-Lozinskii OB, Klochkov LA, Lobunets TF, Raichenko AI, et al. Field assisted sintering of nanocrystalline titanium nitride powder. *Powder Metall Met Ceram*. 2011;50(3):157. <https://doi.org/10.1007/s11106-011-9313-1>
72. Kauffmann F, Ji B, Dehm G, Gao H, Arzt E. A quantitative study of the hardness of a superhard nanocrystalline titanium nitride/silicon nitride coating. *Scr Mater*. 2005;52(12):1269–74. <https://doi.org/10.1016/j.scriptamat.2005.02.024>
73. He JL, Setsuhara Y, Shimizu I, Miyake S. Structure refinement and hardness enhancement of titanium nitride films by addition of copper. *Surf Coat Technol*. 2001;137(1):38–42. [https://doi.org/10.1016/S0257-8972\(00\)01089-6](https://doi.org/10.1016/S0257-8972(00)01089-6)
74. Chen X-Q, Niu H, Li D, Li Y. Modeling hardness of polycrystalline materials and bulk metallic glasses. *Intermetallics*. 2011;19(9):1275–81. <https://doi.org/10.1016/j.intermet.2011.03.026>
75. Gallagher PK, Sinclair WR. Oxidation of polycrystalline niobium nitride. *Israel J Chem*. 1982;22(3):222–6. <https://doi.org/10.1002/ijch.198200044>
76. Adams JR, Kramer DK. A study of the oxidation of tantalum nitride by ellipsometry and auger electron spectroscopy. *Surf Sci*. 1976;56:482–7. [https://doi.org/10.1016/0039-6028\(76\)90469-6](https://doi.org/10.1016/0039-6028(76)90469-6)
77. Brauer G, Weidlein JR. Synthesis and properties of tantalum oxide nitride, TaON. *Angew Chem International Edition in English*. 1965;4(10):875–875. <https://doi.org/10.1002/anie.196508751>
78. Garg SP, Krishnamurthy N, Awasthi A, Venkatraman M. The O-Ta (Oxygen-Tantalum) system. *J Phase Equilibria*. 1996;17(1):63–77. <https://doi.org/10.1007/BF02648373>
79. Murray JL, Wriedt HA. The O–Ti (Oxygen-Titanium) system. *J Phase Equilibria*. 1987;8(2):148–65. <https://doi.org/10.1007/BF02873201>
80. Alper AM. High temperature oxides: oxides of rare earths, titanium, zirconium, hafnium, niobium and tantalum. New York, NY: Academic Press; 1970. 5(2).
81. Perfler L, Kahlenberg V, Wikete C, Schmidmair D, Tribus M, Kaindl R. Nanoindentation, high-temperature behavior, and crystallographic/spectroscopic characterization of the high-refractive-index materials  $TiTa_2O_7$  and  $TiNb_2O_7$ . *Inorg Chem*. 2015;54(14):6836–48. <https://doi.org/10.1021/acs.inorgchem.5b00733>
82. Waring JL, Roth RS. Effect of oxide additions on polymorphism of tantalum pentoxide (system  $Ta_2O_5$ – $TiO_2$ ). *J Res Natl Bur Stand Sec*. 1968;72A(2):175
83. Roth RS, Coughanour LW. Phase equilibrium relations in the systems titania-niobia and zirconia-niobia. *J Res Natl Bur Stand*. 1955;55(4):209–13.
84. Kim JO, Achenbach JD, Mirkarimi PB, Shinn M, Barnett SA. Elastic constants of single-crystal transition-metal nitride films measured by line-focus acoustic microscopy. *J Appl Phys*. 1992;72(5):1805–11. <https://doi.org/10.1063/1.351651>
85. Andrievsky AR, Spivak II. Prochnost' tugoplavkikh soedinenii i materialov na ikh osnove. Sprav. Izdanie: Chelabinsk, Mettalurgia; 1989. p. 368.
86. Xiao-Jia C, Viktor VS, Zhigang W, Maddury S, Jiang Q, Simon K, et al. Hard superconducting nitrides. *Proc Natl Acad Sci*. 2005;102(9):3198–201.
87. Vijgen ROE, Dautzenberg JH. Mechanical measurement of the residual stress in thin PVD films. *Thin Solid Films*. 1995;270(1–2):264–9. [https://doi.org/10.1016/0040-6090\(95\)06984-4](https://doi.org/10.1016/0040-6090(95)06984-4)
88. Gispert MP, Serro AP, Colaço R, Pires E, Saramago B. Wear of ceramic coated metal-on-metal bearings used for hip replacement. *Wear*. 2007;263(7–12):1060–5. <https://doi.org/10.1016/j.wear.2006.11.036>
89. Kuwahara H, Mazaki N, Takahashi M, Watanabe T, Yang X, Aizawa T. Mechanical properties of bulk sintered titanium nitride ceramics. *Mater Sci Eng A*. 2001;319:687–91. [https://doi.org/10.1016/S0921-5093\(01\)00936-4](https://doi.org/10.1016/S0921-5093(01)00936-4)
90. Yamada T, Shimada M, Koizumi M. Fabrication and characterization of titanium nitride by high-pressure hot-pressing. *Am Ceram Soc Bull*. 1980;59(6):611.
91. Moriyama M, Kamata K, Kobayashi Y. Mechanical and electrical properties of hot-pressed TiN ceramics without additives. *J Ceram Soc Jpn*. 1991;99(1148):286–91. <https://doi.org/10.2109/jcersj.99.286>
92. Muchiri PW, Mwalukulu VM, Korir KK, Amolo GO, Makau NW. Hardness characterization parameters of niobium carbide and niobium nitride: a first principles study. *Mater Chem Phys*. 2019;229:489–94. <https://doi.org/10.1016/j.matchemphys.2019.03.001>
93. Marlo M, Milman V. Density-functional study of bulk and surface properties of titanium nitride using different exchange-correlation functionals. *Phys Rev B*. 2000;62(4):2899. <https://doi.org/10.1103/PhysRevB.62.2899>
94. Mohammadpour E, Altarawneh M, Al-Nu'airat J, Jiang Z-T, Mondinos N, Dlugogorski BZ. Thermo-mechanical properties of cubic titanium nitride. *Mol Simul*. 2018;44(5):415–23. <https://doi.org/10.1080/08927022.2017.1393810>
95. Liu K, Zhou X-L, Chen H-H, Lu L-Y. Structural and elastic properties of TiN under high pressure. *Physica B Condens Matter*. 2012;407(17):3617–21.
96. Amriou T, Bouhafs B, Aourag H, Khelifa B, Bresson S, Mathieu C. FP-LAPW investigations of electronic structure and bonding mechanism of NbC and NbN compounds. *Physica B Condens Matter*. 2003;325:46–56. [https://doi.org/10.1016/S0921-4526\(02\)01429-1](https://doi.org/10.1016/S0921-4526(02)01429-1)
97. Da-Hua R, Xin-Lu C. First-principles calculations on the elastic and thermodynamic properties of NbN. *Chin Phys B*. 2012;21(12):127103. <https://doi.org/10.1088/1674-1056/21/12/127103>
98. Li XF, Liu ZL. First-principles investigations of structural and electronic properties of niobium nitrides under pressures. *J At Mol Sci*. 2012;3(1):78–88. <https://doi.org/10.4208/jams.040911.050711a>
99. Zhao E, Hong B, Meng J, Wu Z. First principles investigation on the ultra-incompressible and hard TaN. *J Comput Chem*. 2009;30(14):2358–63. <https://doi.org/10.1002/jcc.21234>
100. Li J, Wang X, Liu K, Li D, Chen L. Crystal structures, mechanical and electronic properties of tantalum monocarbide and mononitride. *J Superhard Mater*. 2011;33(3):173–8. <https://doi.org/10.3103/S1063457611030051>
101. Ren F, Wang Y. Pressure-induced phase transition of tantalum mononitride. *Thin Solid Films*. 2011;519(11):3954–8. <https://doi.org/10.1016/j.tsf.2011.01.247>
102. Chang J, Zhao G-P, Zhou X-L, Liu K, Lu L-Y. Structure and mechanical properties of tantalum mononitride under high pressure: a first-principles study. *J Appl Phys*. 2012;112(8):083519. <https://doi.org/10.1063/1.4759279>

103. Wu Z, Chen X-J, Struzhkin VV, Cohen RE. Trends in elasticity and electronic structure of transition-metal nitrides and carbides from first principles. *Phys Rev B*. 2005;71(21):214103. <https://doi.org/10.1103/PhysRevB.71.214103>
104. Sahnoun M, Daul C, Driz M, Parlebas JC, Demangeat C. FP-LAPW investigation of electronic structure of TaN and TaC compounds. *Comput Mater Sci*. 2005;33(1–3):175–83. <https://doi.org/10.1016/j.commatsci.2004.12.010>

## SUPPORTING INFORMATION

Additional supporting information may be found online in the Supporting Information section.

**How to cite this article:** Mondal S, Durygin A, Drozd V, Belisario J, Cheng Z. Multicomponent bulk metal nitride ( $\text{Nb}_{1/3}\text{Ta}_{1/3}\text{Ti}_{1/3}\text{N}_{1-\delta}$ ) synthesis via reaction flash sintering and characterizations. *J Am Ceram Soc*. 2020;103:4876–4893. <https://doi.org/10.1111/jace.17226>